Dose-Rate-Effects in XRCC1 Wild-type and Mutant CHO Cell Lines Using An ^{241}Am Source

by

Dwight McCoy Chambers

B.S. Massachusetts Institute of Technology (2007)

Submitted to the Department of Nuclear Science and Engineering
in partial fulfillment of the requirements for the degree of

Master of Science in Nuclear Science and Engineering

at the

MASSACHUSETTS INSTITUTE OF TECHNOLOGY

September 2008

Author . .....
Department of Nuclear Science and Engineering
September 5, 2008

Certified by..... .....
Jacquelin C. Yanch
Professor, Department of Nuclear Science and Engineering
Thesis Supervisor

Read by..... .....
Bevin Engelward
Associate Professor, Department of Biological Engineering
Thesis Reader

Accepted by..... .....
Jacquelin C. Yanch
Chairman, Department Committee on Graduate Students

Dose-Rate-Effects in XRCC1 Wild-type and Mutant CHO Cell Lines Using An ^{241}Am Source

by

Dwight McCoy Chambers

Submitted to the Department of Nuclear Science and Engineering
on September 5, 2008, in partial fulfillment of the
requirements for the degree of
Master of Science in Nuclear Science and Engineering

Abstract

This work explores the effects of low-dose-rate radiation on both the AA8 (wild-type CHO cells) and EM9 (XRCC1 null CHO mutants) cell lines. In particular, this study performed clonogenic survival and growth assays to determine the radiations' effect on the cells proliferative capacity. It was hypothesized that the XRCC1 null mutants would show greater radiosensitivity during continuous low-dose-rate radiation since the inability to rapidly respond to DNA damage would result in the gradual accumulation of cytotoxic double strand DNA breaks and/or chromosome exchanges/aberrations. The cells were irradiated for 7 days with photons from unencapsulated ^{241}Am plate sources for chronic, low-dose-rate studies, at dose-rates between $1.99 \pm .610 \times 10^{-3}$ cGy/h and $1.23 \pm .0325$ cGy/h, and irradiated with a Phillips RT250 X-ray machine at 250 kVp and 2.5 Gy/min to doses between 0.02-10 Gy for acute studies. There were significant differences in the growth rates of the unirradiated controls and the irradiated flasks at all dose-rates for both AA8s and EM9s (except for the EM9 $9.08 \pm .390 \times 10^{-3}$ cGy/h flask where $p<.10$). There were also suggestive ($p<.20$) differences in the clonogenic survival for both cell lines compared to controls with significant ($p<.05$) differences observed in the EM9 irradiated population at dose-rates of: $6.89 \pm .315 \times 10^{-3}$ cGy/h, $3.30 \pm .80 \times 10^{-3}$ cGy/h, and $1.99 \pm .61 \times 10^{-3}$ cGy/h. Moreover, there are suggestive ($p<.15$) trends indicating that XRCC1 deficient cells are more susceptible to chronic low-dose-rate radiation (dose-rates compared were between $1.99 \pm .61 \times 10^{-3}$ cGy/hand $9.08 \pm .39 \times 10^{-3}$ cGy/h) as compared with acute exposures at the same dose. Despite some procedural differences with other published works, these results may be evidence of the "inverse dose-rate" effect noted by other authors.

Thesis Supervisor: Jacquelin C. Yanch
Title: Professor, Department of Nuclear Science and Engineering

Thesis Reader: Bevin Engelward
Title: Associate Professor, Department of Biological Engineering

Acknowledgments

I am fortunate to have so many people to thank for helping me to get where I am today. First and foremost, I would like to thank my brother and my parents. Their love and encouragement is essential to my success. I would also like to sincerely thank Profs. Yanch and Engelward for affording me the opportunity to be a part of this work and mentoring me through the process.

I must also take special care to thank Matt Davidson. Beyond his numerous acts of technical assistance, his fun spirit helped make this an enjoyable project.

I am also grateful to Anurag Maheshwari for his expert assistance.

There are so many people who have made my MIT journey so special that I do not have space to thank you all properly. So, Sigma Nu brothers, rowers, Course 22 Nuclear Family members, office-mates, lab-partners, ex-boyfriends, and friends, please accept my gross group thank you *in lieu* of more personal recognition.

Finally, thank you to Tom Larsen for shaming me into writing this up in LaTeX and offering me the critical assistance necessary to make that a reality. It almost makes up for years of stealing my socks ... almost.

Contents

1 Introduction **21**

1.1 Overview of this work 21

1.2 Literature Review 22

1.2.1 Radiobiology Overview 22

1.2.2 Construction of Low-Dose-Rate Facilities 22

1.2.3 Findings from the Edge: Low-Dose-Rate Phenomena 23

1.2.4 Biological Characterization of AA8 and EM9 Lines 27

1.2.5 Acute AA8-EM9 Clonogenic Survival Studies 27

2 Dosimetry and Experimental Design **31**

2.1 Optically Stimulated Dosimeters 32

2.1.1 Theory 32

2.1.2 Thermal Effects and Quenching 34

2.1.3 Linearity 34

2.1.4 Landauer μStar Dot Dosimeters 35

2.2 Experimental Setup 36

2.2.1 Decay Characteristics of the ^{241}Am Sources 36

2.2.2 Physical Characteristics of the Americium Foils 37

2.2.3 Energy Spectra of the ^{241}Am Sources 39

2.2.4 Dose-Rate Characterization 40

2.2.5 Incubator Arrangement 47

2.2.6 Characteristics of the 250 kVp X-Ray Generator 47

3 Biological Protocols **53**

3.1 Cell Handling and Maintenance 53

3.1.1 Medium Preparation 53

3.1.2 Cell Passaging 54

3.2 Biological Assays 54

3.2.1 Clonagenic Survival Assay 54

3.2.2 CyQUANT Growth Assay 56

4 Results And Discussion **59**

4.1 Results 59

4.1.1 Clonogenic Assay: Continuous and Acute 59

4.1.2 CyQUANT Assay 65

4.2 Discussion 66

List of Figures

1-1 Schematic summarizing the design features of a typical low-dose-rate facility. Shelves in a 9 m × 12 m × 5 m concrete shielded room surround a 370 GBq ^{137}Cs source radially. The dose-rates at several of the distances from the source are noted. Control samples are shielded by a 60 cm thick concrete wall, behind which the dose-rate is the same as it is outside the facility. Because of the mono-energetic nature of the source (a 667 keV γ-ray) and the radiations' long mean free path, the various dose-rate positions generally receive the same radiation energy spectrum [29]. 24

1-2 Induction of HPRT mutations at various dose-rates in a number of different cell lines. $\sqcap$ symbols refer to data from CHO V-79 cells, Δ and x shapes refer to data from TK6 lymphoblastiod, and × refers to mouse lymphoma L5178Y cells. Two parabolic lines, fitting particular cell lines, are shown as well. The data suggest there is a minimally sparing dose-rate for the various cell lines and that dose-rates above and below that point cause more damage [41]. 26

1-3 Clonogenic survival curves from Skov *et al.* for AA8 and EM9 cell lines exposed to 250 kVp x-rays at 0.016 Gy/min-0.44 Gy/min dose-rates. The Figure demonstrates the inferior repair capacity of EM9s with respect to AA8s through the shallowness of the EM9 shoulder and the increased radiosensitivity of EM9s with respect to AA8s through the increased slope of the linear portion of the EM9 curve [32]. 29

2-1 This cartoon shows most of the possible ionization paths in OSL materials. (1) shows a full transition from the valence to conduction band; (2) shows an ionization to a very shallow (and hence, unstable) defect trap; (3a) shows an ionization from a localized defect to the conduction band while (3b) shows an ionization to a deep trap; (4a) illustrates ionizations from a deep trap back into the conduction band; (4b) shows an ionization from the valence band into a localized defect trap; (5) shows a defect to defect transition [9, 22]. 32

2-2 This illustration depicts the possible transitions during optical stimulation of the OSL material. (1) depicts promotion and trapping by a shallow trap while (2) depicts promotion from a more typical OSL defect trap. (3) shows a deep trap into which ions can become localized while (4) and (5) depict radiative and non-radiative recombination centers respectively [9]. 33

2-3 Part (a) of this figure depicts thermal quenching of the OSL signal in Al_2O_3:C. At higher and higher temperatures, more charges are reunited during periods where the OSL is not being stimulated (and observed) or are being reunited through more non-radiative pathways. There is a general region of stability for Al_2O_3:C materials through 400 K [9]. 35

2-4 This figure depicts the linear Al_2O_3:C response to dose from $^{90}Sr/^{90}Y$ β decay. The linear range extends up to 50 Gy for this material. The "weak" and "strong" beam conditions refer to the intensity of laser light used to perturb the meta-stable states in the irradiated crystal. Under both reading conditions, the response is linear [9]. 35

2-5 Crystalline structure of Al_2O_3 with the aluminum ions in grey and the oxygen ions in red. The general structure of the crystal is a series of interlocking hexagons and octagons [13]. 36

2-6 A decay scheme showing likely transitions for ^{241}Am. The probabilities for each transition are given relative to all possible decays and all energies indicated are keV [18]. 38

2-7 Schematic depiction of the ^{241}Am foils manufactured by NRD, LLC. The ^{241}Am powder is mixed with gold and sandwiched between gold, silver and palladium foils. The varying composition and thickness of the surrounding material gives directionality to the radiation quality and dose-rate [45]. 38

2-8 This curve shows the energy dependent efficiency correction that must be applied to raw spectra from the Amptek X123 Sn-PIN spectrometer. While the detector is highly efficient at very low energies, it has low efficiency much above 15 keV. 40

2-9 Energy spectra of Dr. Yanchs ^{241}Am foil (3 of 32). The spectrum was collected on an Amptek X123 Sn-PIN spectrometer for 10 minutes. The raw counts (red) were corrected using the manufacturers energy-efficiency data to produce the adjusted spectrum (blue). 41

2-10 Energy spectrum from Dr. Coderre/s ^{241}Am foil (Coderre-1). The spectrum was collected on an Amptek X123 Sn-PIN spectrometer for 18 hours. The raw counts were corrected using the manufacturers energy-efficiency data to produce the adjusted spectrum (blue). . . . 42

2-11 Energy spectrum from Dr. Coderre/s ^{241}Am foil (Coderre-2). The spectrum was collected on an Amptek X123 Sn-PIN spectrometer for 30 minutes. The raw counts (red) were corrected using the manufacturers energy-efficiency data to produce the adjusted spectrum (blue). . . . 43

2-12 Energy spectrum from Dr. Coderre/s ^{241}Am foil (Coderre-3). The spectrum was collected on an Amptek X123 Sn-PIN spectrometer for 30 minutes. The raw counts were corrected using the manufacturers energy-efficiency data to produce the adjusted spectrum (blue). . . . 44

2-13 Energy spectrum from Dr. Coderre/s ^{241}Am foil (Coderre-4). The spectrum was collected on an Amptek X123 Sn-PIN spectrometer for 90 minutes. The raw counts were corrected using the manufacturer/s energy-efficiency data to produce the adjusted spectrum (blue). While the additional noise is due to the combination of low foil activity and a short measurement time, the underlying energy spectrum of this foil is the same as other foils. 45

2-14 The dose per photon deposited at various depths of polyethylene by ^{241}Am 59.5 keV γ-rays, ^{237}Np x-rays and a mixed source of those two radiations all normalized to the same initial dose/photon value as estimated by an MCNP simulation. In the Figure, it is clear that the ^{237}Np x-rays are less penetrating and are preferentially moderated compared to the ^{241}Am γ-rays. The ^{241}Am plate sources are a combination of these two radiations and behave as their weighted average. This Figure was produced and provided by Matthew Davidson. 46

2-15 The energy spectrum of an ^{241}Am foil from the gold plated side through 0.2 mm of lead shielding. The lead differentially attenuates the low energy ^{237}Np x-rays leaving a field that is dominated by the 59.5 keV γ-ray. This figure is courtesy of Matthew Davidson. 47

2-16 Geometric dose-rate effects as seen on the Coderre-1 foil. The cells are modeled to be in a dish approximately $\frac{1}{16}$ of an inch off the surface of the foil. The foil is 3 inches by 3 inches. 48

2-17 Image of one of Dr. Yanch/s ^{241}Am foils taken with BAS Imaging Plate by An Vu. The imaging plate has a spatial resolution of 100 μm^2. . . 48

2-18 Figure depicting the arrangement of the incubator for continuous irradiation experiments. The top shelf holds the higher activity Yanch foils and the smaller, lower activity Coderre foils are on the bottom shelf. The Yanch foils are shielded on their bottoms with 6.35 mm of lead to prevent their radiation from contributing to the dose received by samples on the Coderre foils. 48

2-19 A Figure depicting the gun-stand arrangement in the Phillips RT250 irradiation chamber. The gun is oriented toward the ground and the stand is directly underneath. Markings on the table help to properly orient the stand to minimize position induced variance in the dose delivered by the generator. The stand also has marking on its surface to help orient samples properly. 49

2-20 Dose-Rate as a function of distance as measured by Landauer Dot Dosimeters, Luxel personal dosimeter badges and by previous researchers. All measurements were conducted in a 250 kVp field at 15 mA and into a 0.4 Th target (except the 100 cGy/min Reference point which had a current of 12 mA). The μStar Dots were exposed for 9 minutes while the Luxel badges were exposed for 5 minutes each. Both the badges and the dots have different ratios between their measurements at the 11.25 in. and 9.7 in. stand height positions and the reference dose-rates given at those points. Both the dots and the badges have good fits to a $\frac{1}{r^2}$ curve: $R^2_{dot} = .952$ and $R^2_{badge} = .987$. 51

4-1 A picture of a flask whose colonies are representative of the distribution of colony sizes found on both the AA8 and EM9 clonogenic flasks. While visible to the eye, the largest colonies were often only tenths of a millimeter in diameter. The smaller colonies, which were considerably smaller, had to be compared to a standard sized colony that was counted under a light microscope and found to have approximately 50 cells. The colonies ranged in size, with some of the largest colonies being around 0.1 mm in diameter. 60

4-2 Colony forming assay results for AA8 (red) and EM9 (blue) cells exposed acutely to a 250 kVp x-ray field and allowed to grow for 7 days. The x-ray dose-rate was 2.5 Gy/min with doses between 0.02 Gy and 10 Gy as reported in Table 4.2. The survival data were fit with both a "multi-target single hit" (MTSH) model and a "linear-quadratic" model. For the linear-quadratic model, the AA8 cell lines $\alpha = 0.5656$, $\beta = 0$, and the goodness of fit, as assessed by R^2, was 0.8941. The parameters for the EM9 fit are: $\alpha = 1.498$, $\beta = 0$, and $R^2 = .9144$. For the MTSH model, the parameters for the AA8 fit are: $n = 1$, $D_0 = 1.768$ and $R^2 = 0.8941$. The parameters for the EM9 fit are: $n = 1$, $D_0 = 0.6675$, and $R^2 = .9144$. These two models are reducible to each other in the form: $y(D) = e^{\frac{-D}{D_0}}$ where D_0 is $\frac{1}{\alpha}$. The error bars are calculated based on the Poisson "counting" error associated with random processes. 62

4-3 Colony forming assay results for AA8 and EM9 cells exposed chronically to low-dose-rate radiation from ^{241}Am sources for 7 days. The dose-rates, as reported in Table 4.2, range from 0.00199 ± 0.00061 cGy/h to 1.23 ± 0.03 cGy/h. There is a pronounced difference between the survival of the AA8 and EM9 pairs at all dose-rates. There is also a lack of conclusive dose-rate structure to both curves as seen by the hypothesis testing reported in Table 4.3. The error bars represent the error derived from a technical repeat at each dose-rate (except on the $9.08 \pm .390 \times 10^{-3}$ cGy/h (Coderre-2) foil in which case no error bars are indicated). 63

4-4 A bar chart summarizing the average number of AA8 and EM9 cells in at least five wells at each dose-rate after 4.5 days. The error bars are based on the pooled error from 5 technical repeats. Each well was initially plated at a density of 400 cells / well. While there is a significant difference (see Table 4.6) between irradiated and non irradiated samples for each cell line, the inter-cell line differences and cell line differences at any particular dose-rate are not significant. 66

4-5 Clonogenic survival curve for AA8 and EM9 cell lines exposed acutely to 40 kVp x-rays at a dose-rate between 2.2-4 Gy/min. The (D_0, n) for the AA8s and EM9s lines are (1.2, 100) and (0.6, 100) respectively. For both cell lines, a repair shoulder is prominent at the low end of the Dose axis. [35]. 68

List of Tables

1.1 Clonogenic survival parameters for AA8 and EM9 cells line from both "Multi-Target Single Hit" and "Linear Quadratic" models from vanAnkeren *et al.* [40]. 28

2.1 Photons associated with ^{241}Am decay and present in at least 0.1% of all decays [21]. 37

2.2 Summary of the physical characteristics and activities of all the foils in use during the experiment. 39

2.3 Summary of the dose-rates measured from the interior of the ^{241}Am foils gold sides using the μStar Dot Dosimeter System. There are considerable discrepancies in the dose-rate both from the nominal activity provided by NRD and from the α-particle fluence measured by Dr. Rong Wang [27]. 42

4.1 Parameters describing the Linear-Quadratic and Multi-Target Single Hit Models for both cells lines. Despite having different forms, the models' parameters reduce the two models into a single function of the form: $y(D) = e^{\frac{-D}{D_0}}$. R^2 is used to determine how well the models parameters fit the particular data. 60

4.2 Summary of data from continuous and acute clonogenic assays. The colony-forming fraction was computed by dividing the average number of colonies observed at a particular dose or dose- rate by the average number of colonies formed in that particular exposure regime. The individual errors associated with any one condition (as represented by the standard deviation of measurements in that set) were propagated to give the error to the colony-forming fraction. Conditions in bold represent an RBE dose-rate achieved by shielding a Yanch foil with 0.8 mm of lead. 61

4.3 A matrix with the T-values from various intra-cell line comparisons and intra-dose-rate comparisons for the continuous exposure Colony Forming Fraction (CFF) data from Students T-test. The diagonal line compares the AA8 and EM9 fractions at a particular dose-rate. The lower half of the matrix compares a particular EM9 dose-rate to other EM9 dose-rates. The top half of the matrix compares a particular AA8 dose-rate to the other AA8 dose-rates. The p-values for 0.05, 0.10, 0.15, and 0.20 for two degrees of freedom are 2.920, 1.886, 1.386, and 1.061. The dose-rate in bold indicates that the dose-rate was achieved by shielding a Yanch Foil with 0.8 mm of lead and has a 59.5 keV γ-ray dominated energy profile. These T-values indicate that there are significant differences between the control and irradiated population's CFF values for both AA8 and EM9 lines. They also indicate that there are significant differences between the CFF values between AA8 and EM9 lines for any particular dose-rate. However, there do not generally appear to be any significant CFF differences between different dose-rates inside the same cell line. 64

4.4 A table comparing the significance of the differential AA8-EM9 colony forming fraction (CFF) between the continuous and acute exposures for a given dose and the significance of the difference between exposure regimes at any given point for either AA8s or EM9s. Based on models derived for the acute survival data, CFF fractions for the AA8 and EM9 lines were extrapolated for the lowest three dose-rates since the model behaves well in this region. The error associated with these values scales with the goodness of fit metric, R^2. The differences between AA8 and EM9 CFF were then compared across exposure modalities and used to generate a T-value for a paired data ("AA8-EM9 Differential Difference T-Value"). The differences between the CFFs of the two exposure modalities for any one cells line at a particular dose were also tested for both EM9s and AA8s ("Chronic-Acute Difference T-Value"). The p-values for one degree of freedom for 0.05, 0.10, 0.15, and 0.20 are 6.314, 3.078, 1.936, and 1.376. These T-values indicate that there is a significant enhancement of the AA8-EM9 CFF difference between exposure modalities at all dose-rates and a significant difference for the CFFs of AA8s and EM9s between the chronic and acute exposures. . 64

4.5 A table summarizing the results of the CyQUANT growth assay for AA8s and EM9s under various dose-rates. The table reports the number of cells after 4.5 days from an intial plating of 200 cells / well. The errors in the measurements are calculated by the standard deviation of the group of wells in that particular dose-rate. 65

4.6 A matrix with the T-values from various intra-cell line comparisons and intra-dose-rate comparisons for the continuous exposure CyQUANT data from Students T-test. The diagonal line compares AA8 growth behavior to EM9 growth behavior normalized by the negative control for the same dose-rate. The lower half of the matrix compares a particular EM9 dose-rate to other EM9 dose-rates. The top half of the matrix compares a particular AA8 dose-rate to the other AA8 dose-rates. The p-values for 0.05, 0.10, 0.15, and 0.20 for two degrees of freedom are 1.860, 1.397, 1.108, and 0.889. These values indicate that the radiation significantly changes the normal growth rate of each particular cell line, but there are no significant differences among the growth rates of irradiated cells both in lines and in dose-rates in a single line. 67

Chapter 1

Introduction

1.1 Overview of this work

This work will explore the effects of low-dose-rate radiation on both the AA8 (wild-type CHO cells) and EM9 (XRCC1 null CHO mutants) cell lines. In particular, this study will perform clonogenic survival and growth assays to determine the radiations' effect on the cells' proliferative capacity. The cells will be irradiated with unencapsulated ^{241}Am plate sources for chronic, low-dose-rate studies, between $1.99 \pm .610 \times 10^{-3}$ cGy/h and 1.23 ± 0.0325 cGy/h, and irradiated with a Phillips RT250 X-ray machine at 250 kVp and 2.5 Gy/min for acute studies. These results will be used to reach conclusions concerning the effects of low-dose-rate radiation *in vitro* and concerning the importance of the XRCC1 protein in DNA repair in this regime. The acute studies will serve as a point of contrast for the low-dose-rate studies and as a connection to the body of published literature. It is hypothesized that the XRCC1 null mutants will show greater radiosensitivity during continuous low-dose-rate radiation since the inability to rapidly respond to DNA damage will result in the gradual accumulation of cytotoxic double strand DNA breaks and/or chromosome exchanges/aberrations. As part of this work, some preliminary work necessary to compare the relative biological effect (RBE) of the ^{241}Am γ-rays and the ^{237}Np x-rays is also preformed.

1.2 Literature Review

This review will provide an overview of the radiobiological methods and published results for experiments in the low-dose-rate regime. Specifically, this chapter will discuss the construction of large-scale, low-dose-rate facilities and unique radiobiological phenomena that manifest in the low-dose-rate regime. The chapter will conclude with a brief overview of the biological differences and previous clonogenic survival studies conducted on the two CHO cell lines under study, AA8 and EM9.

1.2.1 Radiobiology Overview

Radiation biology studies the intersections between ionizing radiation and biology. The goal of this field is to provide insights into how to evaluate the risks posed by environmental and man-made radiological conditions as well as to help to develop radiologic solutions to various pathological conditions. While there is a strong scientific consensus on the effects of acute, high dose, high dose-rate radiation on biological systems, most living things develop in radiation environment characterized by a chronic background of approximately 3.6 mSv/year (4.1×10^{-4} mSv/hr), 2.53 mSv/year of which comes from a combination of Radon and medical procedures [14]. Currently, the effects of low dose-rate radiation are extrapolated from the well-characterized set of high dose, high dose-rate radiation studies. As the field develops, there is an increasing desire to *directly* study the biological effects of low-dose-rate and low dose radiation. These studies have been catalyzed by the advent of specialized DNA repair mutants that help elucidate the supposedly subtle effects of low-dose-rate radiation. Furthermore, radiation as a cellular and DNA damaging agent has helped provide insights into the basic biology of cell signaling and DNA damage repair through studies of specially designed / isolated mutants.

1.2.2 Construction of Low-Dose-Rate Facilities

Several groups around the world have begun constructing large-scale, low-dose-rate, chronic exposure facilities such as the Low Dose Radiation Research Center at the

Central Research Institute of Electric Power Industry, Tokyo, Japan and the Low-Dose-Rate Irradiation Facility at Colorado State University. These and other such facilities generally exploit a γ-ray source (α or β emitters typically have undesirable range and/or linear energy transfer (LET) characteristics), typically ^{137}Cs or ^{60}Co because of their desirable energy (nearly mono-energetic, penetrating radiation) and half life characteristics (long half lives provide essentially constant dose-rate over the duration of an experiment), and use $\frac{1}{r^2}$ effects to generate various dose-rates [29, 23, 11]. The design of the Japanese facility is shown in Figure 1-1 to give a sense of the materials and distances involved in the construction of a low-dose-rate facility for *in vivo* studies [29]. The same construction principles are used for *in vitro* studies except that additional constrains must be taken to maintain the correct atmosphere and temperature conditions inside the irradiation chamber [23, 11]. This can typically be achieved by placing the cells on a variable height table inside an incubator with a shuttered high activity source [11].

There are other research groups pursuing alternative low-dose-rate designs to the γ-ray facilities described above. One group in France is conducting *in vitro* studies using cells cultured directly on top of a thin layer of thorium nitrate crystals, achieving dose-rates as low as 40 mrad/day [12]. A Japanese group introduced tritiated water (HTO) water directly into the cell medium and achieved dose-rates between 5 cGy/h and 40 cGy/h [38]. While these alternative solutions give the researcher additional flexibilities in terms of radiation types and qualities over the more standard γ-ray sources, they are often burdened by issues of source homogeneity and stability [38].

1.2.3 Findings from the Edge: Low-Dose-Rate Phenomena

Given the number of cell types available, the diversity of radiation sources, and the resolution of biological tools from the level of populations to DNA sequences, it is difficult to provide a complete summary of all the activity occurring in the field of low-dose-rate radiation. That said, there are a number of important phenomena that manifest at low-dose-rates including: dose-rate sparing, sub-limiting dose-rates,

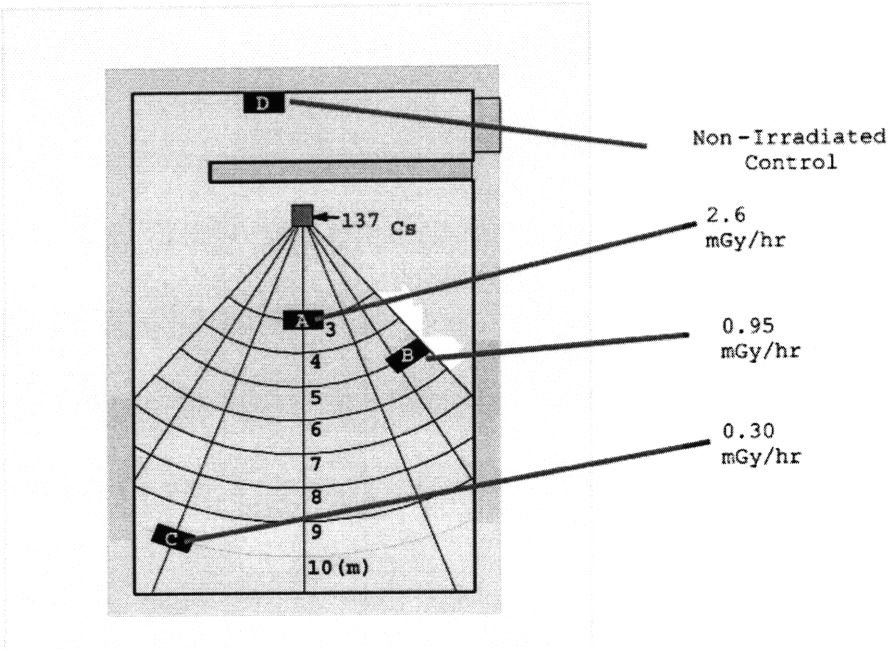

Figure 1-1: Schematic summarizing the design features of a typical low-dose-rate facility. Shelves in a 9 m × 12 m × 5 m concrete shielded room surround a 370 GBq ^{137}Cs source radially. The dose-rates at several of the distances from the source are noted. Control samples are shielded by a 60 cm thick concrete wall, behind which the dose-rate is the same as it is outside the facility. Because of the mono-energetic nature of the source (a 667 keV γ-ray) and the radiations' long mean free path, the various dose-rate positions generally receive the same radiation energy spectrum [29].

radiation hormesis, and inverse dose-rate effects.

Dose-rate sparing or the "dose-rate effect" is the idea that the radiation end-points are correlated to the intensity of the radiation source. This effect is the most commonly observed low-dose-rate phenomenon, seen across most cell types and biological assays. For example, many studies have observed a decrease in cell killing [38, 25, 4, 44], micronuclei induction [8, 42, 38], growth rates retardation [12, 43], mutation induction [20], and γ-H2AX foci induction [19] as the dose-rate of the radiation is lowered. This effect is not unique to low-dose-rate radiation and similar effects are observed from variable high-dose-rate and dose fractionation studies [15]. Dose-rate sparing is often used as evidence of a deterministic (as opposed to stochastic) model of radiation interactions [6].

Other groups have found dose-rates for acute exposures beneath which there are no radiation-induced effects. This threshold is referred to as the sublimiting dose-rate. For example, some authors report critical radiation dose-rates for various lines necessary to induce some survival reaction or inhibit cell division completely. For CHO V79 cells, one group found no clonogenic survival effects were observed below 37 cGy/h while cell division were only completely inhibited at rates above 90 cGy/h [6, 28]. The same group found, for HeLa cells, that division was inhibited at 38 cGy/h [6]. Interestingly, researchers also found that the sublimiting clonogenic dose is often specific to a particular phase of the cell cycle. G2 cell cycle blocks can be accomplished at doses as low as 9 cGy as compared to doses of 300-500 cGy necessary to inhibit division in G1 or S phase [6].

Radiation hormesis is the idea that radiation exposure may have benign or even beneficial effects for living organisms [15]. A number of hormetic effects have been observed by the research group (PI K. Sakai) operating out of the Low Dose Radiation Research Center at the Central Research Institute of Electric Power Industry, Tokyo, Japan. Their findings and related work done by other groups, done with ^{137}Cs γ-rays, include optimal radiation induce tumor suppression at 1 mGy/h [34, 29], life-lengthening in mice with auto-immune disorders at approximately 0.35 mGy/h and 1.2 mGy/h [16] and in healthy populations at approximately 7-14 cGy/year [1], suppression of murine AIDS [31] and a general stimulation of the immune system [30]. Generally, the hypothesis is that low-dose-rate radiation can stimulate the body's natural DNA repair and defense mechanisms while not introducing serious damage [37]. It is worth noting that most (if not all) of the Sakai group findings have been conducted *in vivo* and may not be reproducible *in vitro* if there are higher order biological signaling and phenomena helping to organize the bodily reaction to the radiological insert.

The inverse dose-rate effect is the hypothesis that a decrease in dose-rate leads to an increase in the magnitude of the biological endpoint. This seemingly counter-intuitive

theory has been demonstrated experimentally by Mitchell in clonogenic survival studies with an explanation that the irradiated cells were becoming trapped in an infinite repair loop in a radiosensitive cell cycle phase [23]. More recent work by Vilenchik and Knudson has sought to synthesize dose-rate sparing and the inverse dose-rate effect into a coherent picture of repair activity inside a cell. In this new framework, cells are thought to only be able to detect levels of insult above the rate of endogenous DNA damage. Thus, dose-rates below a certain critical level damage the cell/s DNA while remaining below the repair radar - giving rise to a parabolically shaped DNA damage versus dose-rate curve. An example of such a curve for the induction of mutations in the HPRT locus is shown in Figure 1-2, although their paper extends the analysis to other mutagenic endpoints as well [41]. It is interesting to note that despite the difference in cell lines, all the lines have an inflection point around 1 cGy/min for mutations to the HPRT locus [41].

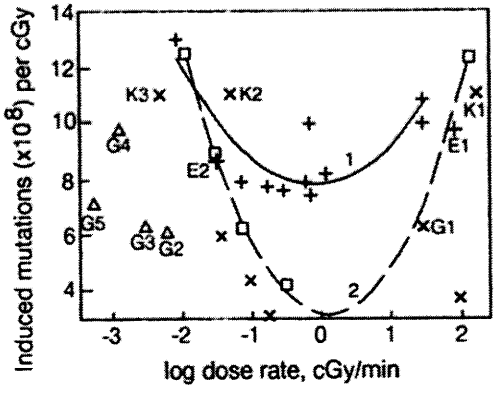

Figure 1-2: Induction of HPRT mutations at various dose-rates in a number of different cell lines. $\sqcap$ symbols refer to data from CHO V-79 cells, Δ and x shapes refer to data from TK6 lymphoblastiod, and $\times$ refers to mouse lymphoma L5178Y cells. Two parabolic lines, fitting particular cell lines, are shown as well. The data suggest there is a minimally sparing dose-rate for the various cell lines and that dose-rates above and below that point cause more damage [41].

1.2.4 Biological Characterization of AA8 and EM9 Lines

In the early 1980s, a research group at Lawrence Livermore National Laboratory led by L.H. Thompson isolated a CHO mutant, labeled EM9, through the use of an ethyl methanesulfonate (EMS) screen from a wild-type CHO line, AA8 [35, 32]. Originally notable for having a 10-fold higher sensitivity to EMS as compared to its parent, AA8, the EM9 line was discovered to have an increased sensitivity to ionizing radiation and other chemical mutagens as well as a much higher endogenous rate of sister-chromatid exchanges [35].

Based on its sensitivity to particular DNA damaging agents, researchers classified EM9 as a single strand break (SSB) and/or base-excision repair (BER) mutant. More specifically, they found that normal CHO cells had a fast followed by slow phase of SSB repair and that EM9 cells were particularly inefficient at executing the fast phase of SSB repair as compared to AA8s [2]. The kinetics of this repair deficiency have been shown to be modulated by several experimental factors including pH [40] and oxygen level [28].

Later, additional work by Thompson identified the X-ray repair cross complementing protein 1 (XRCC1) as the defective protein in the EM9 cell line [36]. XRCC1 appears to have a conserved function in the human genome and is involved with a complex of proteins including: DNA ligase III, polymerase β, and poly (ADP-ribose) polymerase [40]. While the biochemical picture is still incomplete for XRCC1, there is some evidence that it is associated with DNA ligase III. Specifically, purification techniques such as immobilized metal ion affinity chromatography (IMAC) revealed that DNA ligase III and XRCC1 copurify, indicating a biochemical or physical connection between the two proteins [10].

1.2.5 Acute AA8-EM9 Clonogenic Survival Studies

Many different research groups have characterized the clonogenic survival after acute irradiation of both AA8s and EM9s. Shortly after isolating the pair, Thompson

Table 1.1: Clonogenic survival parameters for AA8 and EM9 cells line from both "Multi-Target Single Hit" and "Linear Quadratic" models from vanAnkeren *et al.* [40].

Cell Line	D_0 (Gy)	n	D_e (Gy)	α (Gy^{-1})	β (Gy^{-2})
AA8	1.11 ± 0.08	18.2 ± 3.6	3.22 ± 0.68	0.189 ± 0.016	0.036 ± 0.0018
EM9	1.03 ± 0.04	4.0 ± 0.9	1.43 ± 0.32	0.559 ± 0.014	0.0365 ± 0.002

studied their survival in a 40 kVp X-ray field administered at approximately 2.2-4 Gy/min. His group fit the data to a "Multi-Target Single Hit" (MTSH) Model and reported (D_0,D_e) parameters of (0.6 Gy, 2.9 Gy) and (1.2 Gy, 5.3 Gy) for EM9s and AA8s, respectively [35]. A group, vanAnkeren *et al.*, used AA8 and EM9 survival curves from a 5.0 Gy/min ^{137}Cs source to compare the predictions of the MTSH and "Linear Quadratic" survival models. Their survival parameters are summarized in Table 1.1 [40].

Some groups have even been exploring AA8 and EM9 clonogenic survival at dose-rates approaching the low-dose-rate limit. Skov *et al.* used a 250 kVp x-ray field with dose-rates between 0.016 Gy/min 0.44 Gy/min with doses between 0-2 Gy. While they fit their data to a repair-misrepair (RMR) model, they did not report their parameters. One of their figures is reproduced in Figure 1-3 [32].

General findings from these groups show that EM9s have inferior repair kinetics (as evidenced by the width of the cell survival curve shoulder) and increased radiosensitivity (as evidenced by smaller D_0 values) as compared to the AA8 line.

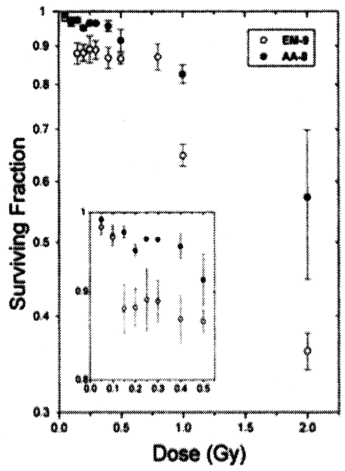

Figure 1-3: Clonogenic survival curves from Skov *et al.* for AA8 and EM9 cell lines exposed to 250 kVp x-rays at 0.016 Gy/min-0.44 Gy/min dose-rates. The Figure demonstrates the inferior repair capacity of EM9s with respect to AA8s through the shallowness of the EM9 shoulder and the increased radiosensitivity of EM9s with respect to AA8s through the increased slope of the linear portion of the EM9 curve [32].

Chapter 2

Dosimetry and Experimental Design

This chapter will explore the characteristics of the dosimetry and radiological systems used in this study. Since the dosimeters are a critical piece of equipment for measuring the dose and dose-rate enviroment, fully exploring their qualities is necessary. This section will begin by summarizing the theoretical behavior of Al_2O_3:C, the dosimetry material used in this work, as an optically stimulated dosimeter and work towards addressing practical aspects of this material in the radiation environment. The dosimetry section will conclude with a discussion of the specifics of the Landauer InLight μStar Dot Dosimetry system. The section on experimental design will open with a summary of the decay process for ^{241}Am and then describe the physical, spectral and dose-rate qualities of the radiative foils used. The design summary will also describe how incubator space was managed and conclude by detailing the spectral and dose-rate characteristics of the X-ray generator used for acute experiments.

2.1 Optically Stimulated Dosimeters

2.1.1 Theory

Generally, the theory of optically stimulated luminescence (OSL) relies on the perturbation of the electronic ground state to some meta-stable state, which will, after the introduction of additional perturbation, return to the group state while radiating [9, 22, 3]. More specifically, the OSL materials rely on the electronic structure present in most electrically insulating and semi-conducting material. Incident radiation, mainly through photoelectric or Compton scattering mechanisms, will impart sufficient energy to promote a valence band electron (or to an electron already in a band-gap state) either directly into the conduction band or into some band-gap "defect" electron trap [9]. All possible ionization paths considered during ionization are shown in Figure 2-1.

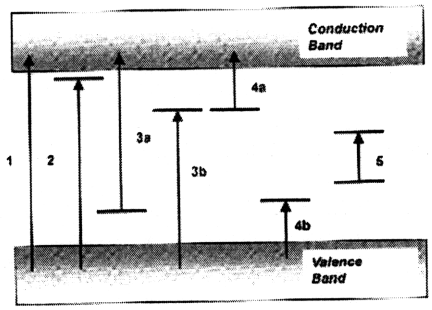

Figure 2-1: This cartoon shows most of the possible ionization paths in OSL materials. (1) shows a full transition from the valence to conduction band; (2) shows an ionization to a very shallow (and hence, unstable) defect trap; (3a) shows an ionization from a localized defect to the conduction band while (3b) shows an ionization to a deep trap; (4a) illustrates ionizations from a deep trap back into the conduction band; (4b) shows an ionization from the valence band into a localized defect trap; (5) shows a defect to defect transition [9, 22].

The promoted electrons will come to settle in some meta-stable energy state created by naturally occurring defects in the crystal/s electric structure [9]. A slight perturbation (usually in the form of coherent light) will re-promote these meta-stable states, allowing them the chance to recombine with their opposite charge carriers (electrons

and electron-holes are the two typical charge carriers). Some of these recombination events are radiative decays and emit characteristic light [9, 22]. A general summary of the stimulation pathways is illustrated in Figure 2-2.

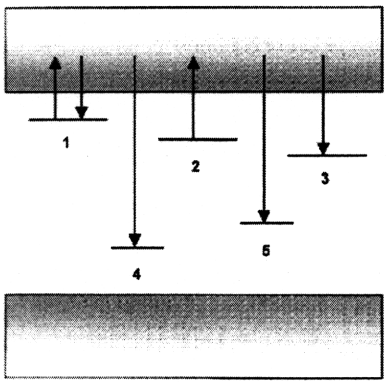

Figure 2-2: This illustration depicts the possible transitions during optical stimulation of the OSL material. (1) depicts promotion and trapping by a shallow trap while (2) depicts promotion from a more typical OSL defect trap. (3) shows a deep trap into which ions can become localized while (4) and (5) depict radiative and non-radiative recombination centers respectively [9].

To a first order approximation, the intensity of an OSL signal, I_{OSL}, is proportional to the dose absorbed during irradiation, D (discussed later in the Linearity Section). The signal intensity is also proportional to the decay rate of μ, the meta-stable states originally induced. This, in turn, is proportional to the number of charge pairs created and the probability of a single pair recombining. The probability, p, of a recombination event is expressed as $\Phi(E)\sigma(E)$ where $\Phi(E)$ is the intensity of stimulating light with energy, E, and $\sigma(E)$ is the photo-interaction cross section for that material at that particular energy (there is also an assumption that E is equal to or greater than the band-gap necessary to liberate the trapped charge) [9]. Equation 2.1 summarizes these relationships:

$$I_{OSL} \propto D \propto |\frac{\delta\mu}{\delta t}| \propto \mu * \Phi(E) * \sigma(E) \tag{2.1}$$

2.1.2 Thermal Effects and Quenching

Besides optical stimulation, OSL material can be thermally stimulated [9, 22, 3]. Generally, the effect of higher temperatures is to destabilize the meta-stable states formed during the initial irradiation [9, 22]. Often, these states are destabilized through some non-radiative pathway [9] or during some time when the resultant luminescence is not detected [9, 22]. Both of these effects contribute to the thermal quenching of OSL materials. Seemingly counter-intuitive, an increase in temperature during optical stimulation can increased the observed signal since additional meta-stable states are destroyed during a period of observation [9]. These effects may be important to *in vitro* studies particularly if measurements are being done in both a room temperature and incubator environment. However, for Al_2O_3:C dosimeters, the temperature difference required for noticeable thermal effects is much larger than discrepancy between these two environments. Figure 2-3 illustrates the relative temperature stability of the Al_2O_3:C detectors in the experimental range. As seen from Figure 2-3, both room temperature and the incubator are in a linear temperature response phase. Over the course of approximately 75 K (350 K to 425 K), the intensity of the material only drops off by 10% [9]. This would imply that the variation of 13 K (between room temperature and the incubator temperature) would cause at most a 1.7% variation in the reported dose.

2.1.3 Linearity

One powerful feature of Al_2O_3:C is the large linear range for OSL signal response to incident radiation. The linear range extends from approximately 10 mrad up to 50 Gy. After 50 Gy, there is a saturation effect and non-linear calibration techniques must be used to extend the dynamic range of the material [9]. Figure 2-4 shows experimental confirmation of the linear response of the Al_2O_3:C dosimeters to doses up to 10 Gy.

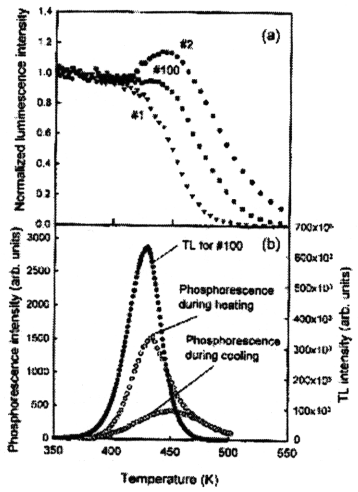

Figure 2-3: Part (a) of this figure depicts thermal quenching of the OSL signal in Al_2O_3:C. At higher and higher temperatures, more charges are reunited during periods where the OSL is not being stimulated (and observed) or are being reunited through more non-radiative pathways. There is a general region of stability for Al_2O_3:C materials through 400 K [9].

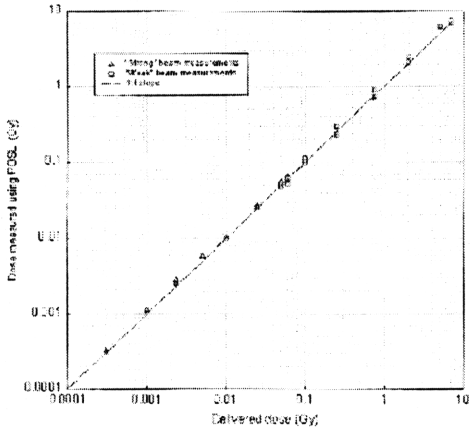

Figure 2-4: This figure depicts the linear Al_2O_3:C response to dose from $^{90}Sr/^{90}Y$ β decay. The linear range extends up to 50 Gy for this material. The "weak" and "strong" beam conditions refer to the intensity of laser light used to perturb the metastable states in the irradiated crystal. Under both reading conditions, the response is linear [9].

2.1.4 Landauer μStar Dot Dosimeters

The specific OSL dosimetry system used for this experiment was the InLight μStar Dot Dosimetry system (Landauer, Glenwood, IL). This system uses small Al_2O_3:C

chips, encased in plastic as the OSL material. To prevent any photo-bleaching from other light sources, the Al_2O_3:C chips are always enclosed in this plastic slip except when being measured. Figure 2-5 is a representation of the Al_2O_3:C material. The chips are approximately 0.75 cm in diameter and the plastic casing is approximately 2.5 cm by 1 cm in size. After irradiation (either at 37oC or at room temperature), the chips are read in a tabletop system that opens the plastic casing and exposes the dosimeter chip to pulses of laser light [33]. The resulting luminescent intensity is reported to Landauer software on an attached PC computer. The dots have been calibrated in a filtered 80 kVp x-ray field (average energy of 44 keV) [33]. After use, the dots are opened and photo-bleached on the FujiFilm IP Eraser (Stamford, CT).

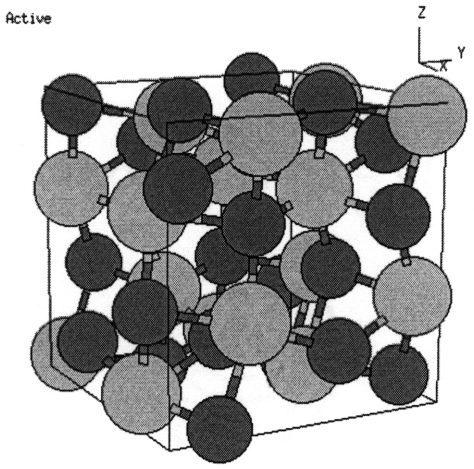

Figure 2-5: Crystalline structure of Al_2O_3 with the aluminum ions in grey and the oxygen ions in red. The general structure of the crystal is a series of interlocking hexagons and octagons [13].

2.2 Experimental Setup

2.2.1 Decay Characteristics of the ^{241}Am Sources

^{241}Americium is an alpha emitter with a half-life of 432.2 years. [21]. While transiting to the ^{237}Np ground state, the Americium nucleus can be left in a variety of meta-stable states that quickly decay through the emission of γ-rays. Most promi-

nent among the possible γ-rays, a 59.5 keV photon is observed in 35.9% of decays [21, 7]. The Neptunium nucleus can also be left in an excited state, which decays through internal conversion. Accordingly, there are a number of low energy X-rays and higher energy γ-rays associated with the decay of ^{241}Am [7, 18]. Table 2.1 summarizes the photon energies that occur in more that 0.1% of all ^{241}Am decays [21]. The predominant decay modes for ^{241}Am are summarized in Figure 2-6.

Table 2.1: Photons associated with ^{241}Am decay and present in at least 0.1% of all decays [21].

Photon Energy (keV)	Source	Branching Ratio (%)
11.871	Np L (1)	0.66
13.761	Np L (a2)	1.07
13.946	Np L (a1)	9.6
15.861	Np L (h)	0.153
16.109	Np L (b6)	0.184
16.816	Np L (b2)	2.5
17.505	Np L (b5)	0.65
17.751	Np L (b1)	5.7
17.992	Np L (b3)	1.37
20.784	Np L (g1)	1.39
21.099	Np L (g2)	0.65
21.342	Np L (g3)	0.59
21.491	Np L (g6)	0.29
26.3448	^{241m}Am	2.4
33.1964	^{241m}Am	0.126
59.5412	^{241m}Am	35.9

2.2.2 Physical Characteristics of the Americium Foils

Five different radiological conditions were created through the use of sources provided by Drs. Jacquelyn Yanch and Jeffrey Coderre. All sources, manufactured by NRD (Grand Island, NY), sandwiched ^{241}Am powder between a series of gold, palladium and silver sheets as illustrated in Figure 2-7.

The foils vary considerably in size and activity per unit area. Dr. Yanch/s foils, an identical set of 32 foils created from 2.17 Ci of ^{241}Am, are 14 inches by 3 inches with

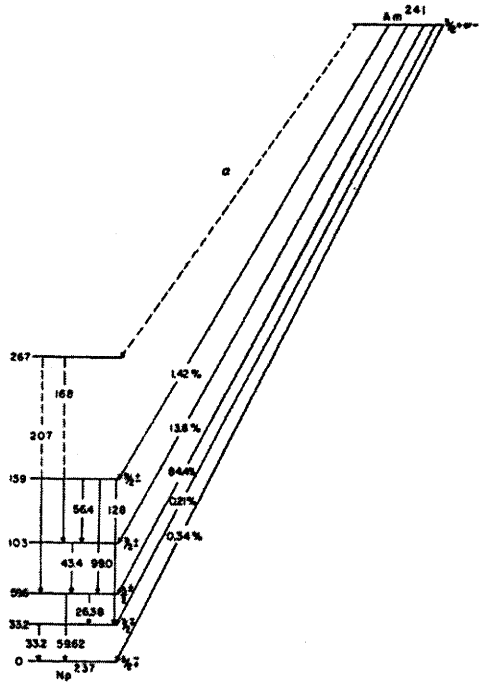

Figure 2-6: A decay scheme showing likely transitions for ^{241}Am. The probabilities for each transition are given relative to all possible decays and all energies indicated are keV [18].

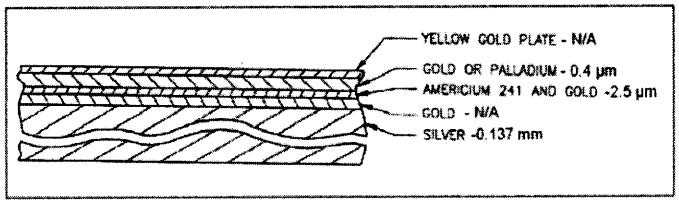

Figure 2-7: Schematic depiction of the ^{241}Am foils manufactured by NRD, LLC. The ^{241}Am powder is mixed with gold and sandwiched between gold, silver and palladium foils. The varying composition and thickness of the surrounding material gives directionality to the radiation quality and dose-rate [45].

an area activity of 250 $\frac{\mu Ci}{cm^2}$. Most of Dr. Coderre/s four foils are 135 cm^2 (one foil is 58 cm^2) with reported nominal area activities of 135 $\frac{\mu Ci}{cm^2}$, 13.5 $\frac{\mu Ci}{cm^2}$, 1.35 $\frac{\mu Ci}{cm^2}$, and one foil with unreported activity. The activity per area and dimensions of all the foils are summarized in Table 2.2.

Table 2.2: Summary of the physical characteristics and activities of all the foils in use during the experiment.

Source Name	Size	Nominal Area Activity ($\frac{\mu Ci}{cm^2}$)
Yanch 1-32	3 in. × 14 in.	250
Coderre 1	3 in. × 3 in.	Unknown
Coderre 2	3 in. × 7 in.	135
Coderre 3	3 in. × 7 in.	13.5
Coderre 4	3 in. × 7 in.	1.35

2.2.3 Energy Spectra of the ^{241}Am Sources

Owing to the similarities in composition and construction, the various Americium foils have very similar energy characteristics. As discussed earlier, the energy spectra are primarily composed of a mixture of ^{241}Am γ-rays and ^{237}Np x-rays. Extraneous photon peaks have been linked to characteristics x-rays from the materials used to encase the sources. The energy spectra were measured using an X123 Si-PIN photodiode spectrometer (Amptek, Bedford, MA) and efficiency adjusted using an energy-efficiency table provided by Amptek [5]. The energy efficiency curve is shown in Figure 2-8. Figures 2-9, 2-10, 2-11, 2-12, and 2-13 are the energy spectra collected from the gold-side of all the ^{241}Am foils. Some figures show the spectra for before and after the energy-efficiency correction is applied.

These collected energy spectra demonstrate conclusively the homogeneity of the energy spectrum across all the radiative foils used in this experiment. A common energy profile is important for isolating the biological effects due solely to a variable dose-rate.

The higher interaction probabilities of the lower energy x-rays compared to the 59.5 keV γ-ray allow for differing qualities of radiation to be observed depending on the distance from the foil through some moderator. That is, the energy spectrum of the source changes through any moderating material. This feature of the sources allows for the construction of doses which are predominately contributed by the ^{237}Np x-rays or predominately composed of the 59.5 keV γ-ray. Figure 2-14 shows the

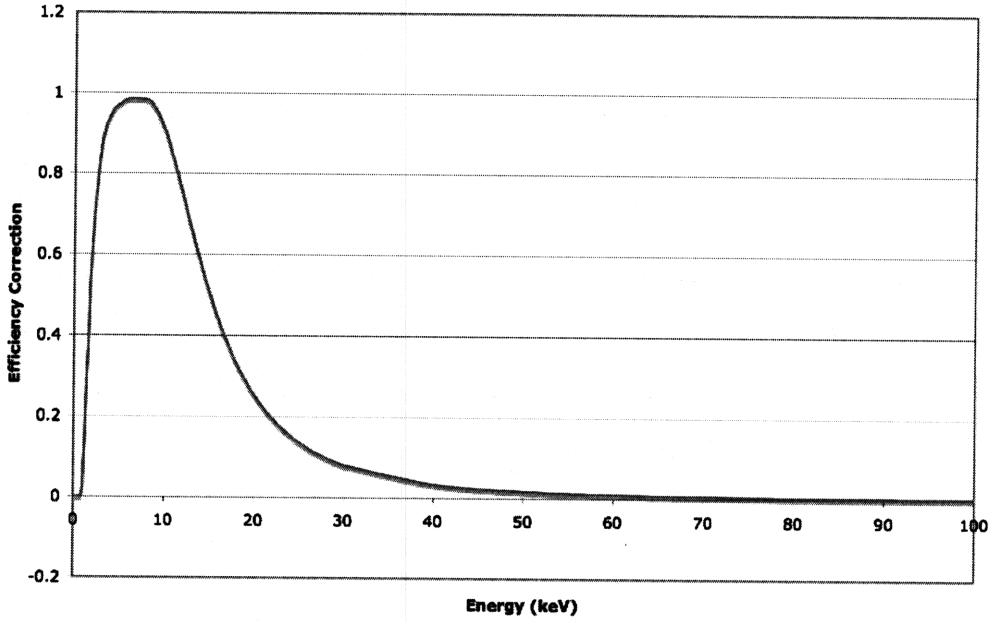

Figure 2-8: This curve shows the energy dependent efficiency correction that must be applied to raw spectra from the Amptek X123 Sn-PIN spectrometer. While the detector is highly efficient at very low energies, it has low efficiency much above 15 keV.

results a MCNP simulation, provided by Matthew Davidson, of the dose deposited by Americium γ-rays and Neptumium x-rays through various depths of polyethylene. The construction of a nearly mono-energetic 59.5 keV γ-ray source is demonstrated experimentally in Figure 2-15. Here, the gold side of the ^{241}Am source was shielded by 0.2 mm of lead before detection in the same X123 Sn-PIN diode detector described earlier. There is clear differential attenuation of the x-rays as compared to the γ-rays. The ability to create two distinct radiation qualities allows for studies that test the relative biological effect (RBE) of the x-rays as compared to the γ-rays.

2.2.4 Dose-Rate Characterization

Two factors influencing the dose-rate to a target on the foils surface are the plate's activity and the geometric considerations of the plate. The dose-rates measured from the center of the plates are summarized in Table 2.3. These dose-rates were measured using the μStar Dot Dosimeters (Landauer, Glenwood, IL) in polystyrene dishes on

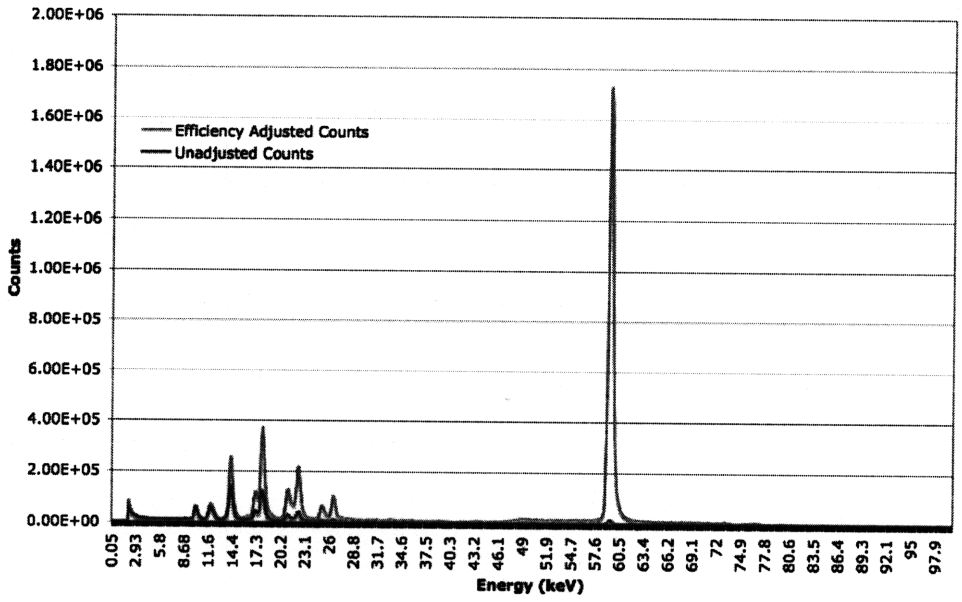

Figure 2-9: Energy spectra of Dr. Yanchs ^{241}Am foil (3 of 32). The spectrum was collected on an Amptek X123 Sn-PIN spectrometer for 10 minutes. The raw counts (red) were corrected using the manufacturers energy-efficiency data to produce the adjusted spectrum (blue).

the gold surface of the foil over a period of ten days. The error in the dose-rate measurement, calculated explicitly in Equation 2.2, is a combination of the interdot (σ_{Group}) and intradot (σ_{Dot}) errors (represented explicitly as the standard deviation of the group of measurements) as each plate was measured using multiple Dots and each Dot was measured multiple times:

$$\sigma_{Total} = \sqrt{\sigma_{Group}^2 + \sigma_{Dot}^2} \tag{2.2}$$

There is considerably less variation in the dose-rate of the plates than is suggested by the difference in the nominal activity per unit area. Moreover, the γ-ray dose-rates do not appear to be linearly correlated to the α-particle dose-rates measured by Dr. Rong Wang with a PIPS detector [27]. The cause of this discrepancy with the nominal activity is unknown and may rest on a misreporting by the manufacturer as to the

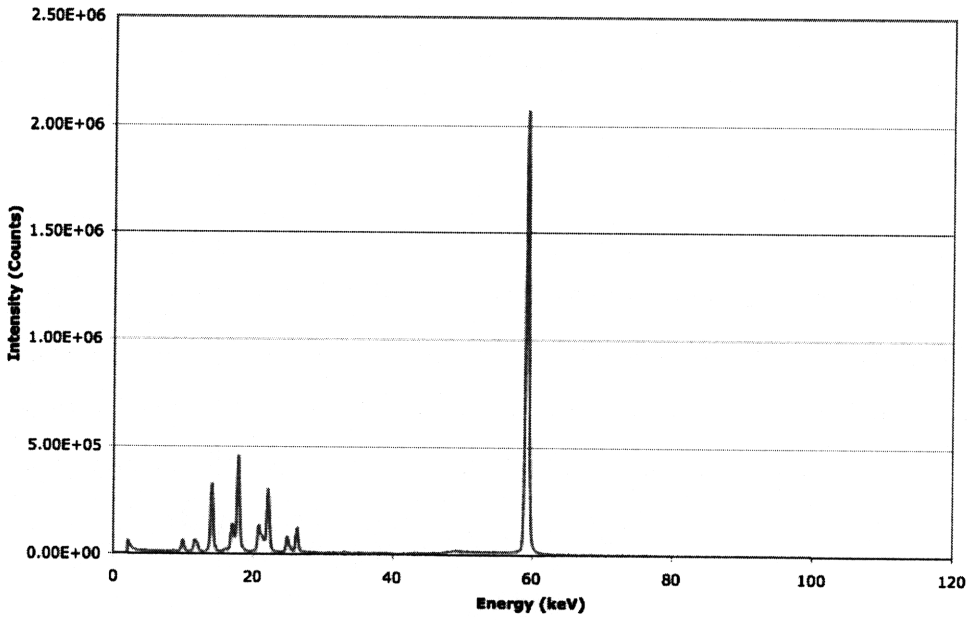

Figure 2-10: Energy spectrum from Dr. Coderre/s ^{241}Am foil (Coderre-1). The spectrum was collected on an Amptek X123 Sn-PIN spectrometer for 18 hours. The raw counts were corrected using the manufacturers energy-efficiency data to produce the adjusted spectrum (blue).

Table 2.3: Summary of the dose-rates measured from the interior of the ^{241}Am foils gold sides using the μStar Dot Dosimeter System. There are considerable discrepancies in the dose-rate both from the nominal activity provided by NRD and from the α-particle fluence measured by Dr. Rong Wang [27].

Source Name	Nominal Area Activity $\frac{\mu Ci}{cm^2}$	Dose-Rate (cGy/h)	Dose-Rate Error (cGy/h)	α Particule Flux $\frac{\alpha}{s-mm^2}$
Yanch - 3/32	250	1.23	3.25×10^{-2}	N/A
Coderre 1	Unknown	4.86×10^{-1}	5.40×10^{-2}	1162.05
Coderre 2	135	9.08×10^{-3}	3.90×10^{-4}	106.72
Coderre 3	13.5	3.30×10^{-3}	8.00×10^{-4}	12.9
Coderre 4	1.35	1.99×10^{-3}	6.10×10^{-4}	3.16

real activity of the plates. The discrepancy with the α-particle fluence measurements appears more serious since the underlying nuclear theory would predict that they two radiation types (photons and α-particles) would be linearly correlated to each other [7].

The dose-rate for the Yanch 3/32 foil, when shielded by 0.8 mm of lead was 6.89 $\pm$ .315 $\times$ 10^{-3} cGy/h as measured by the Dot dosimeters. As seen in Figure 2-15, this thickness of lead was sufficient to create a nearly mono-energetic 59.5 keV γ-ray

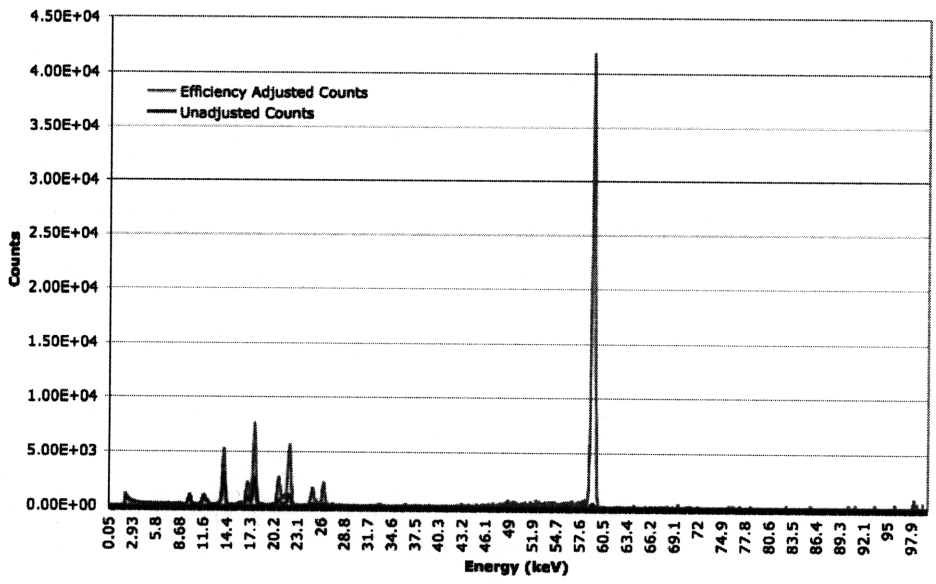

Figure 2-11: Energy spectrum from Dr. Coderre's ^{241}Am foil (Coderre-2). The spectrum was collected on an Amptek X123 Sn-PIN spectrometer for 30 minutes. The raw counts (red) were corrected using the manufacturers energy-efficiency data to produce the adjusted spectrum (blue).

source. This new source was used to qualitatively explore the RBE effect from the x-ray dominated and γ-ray dominated spectra by comparing the clonogenic survival for cells exposed in each radiative field to the other.

The geometric variance in dose-rate arises from the fact that not all positions on the surface of the plate have the same apparent view of the radiation surface. That is, the finite size of the foil introduces variation in dose-rate across its surface. The solid angle is a quantitative measure of this effective change in the surface area of the radiative foil. The general relationship for the solid angle a surface subtends from a given point is given in Equation 2.3:

$$\Omega = \int\int \frac{\vec{r} \cdot \hat{n} dS}{r^3} \tag{2.3}$$

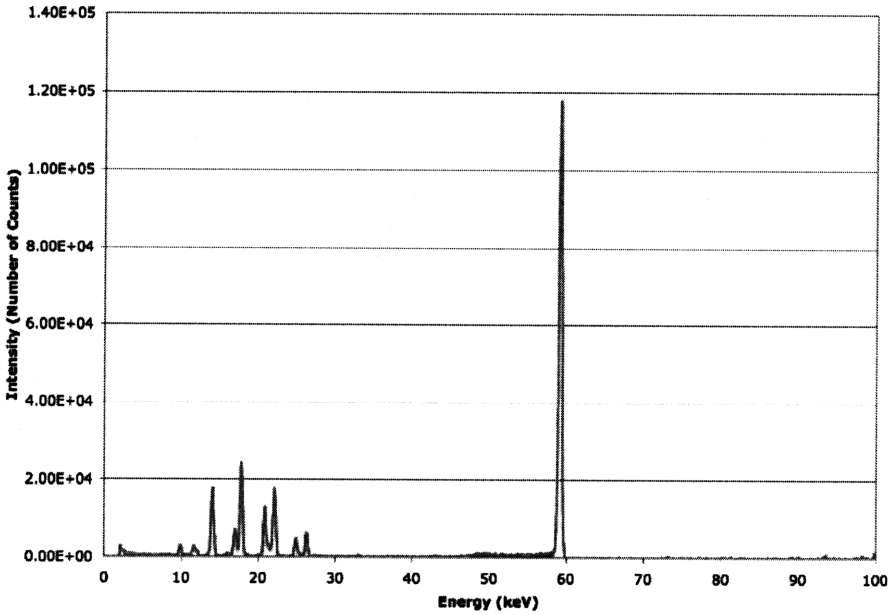

Figure 2-12: Energy spectrum from Dr. Coderre/s ^{241}Am foil (Coderre-3). The spectrum was collected on an Amptek X123 Sn-PIN spectrometer for 30 minutes. The raw counts were corrected using the manufacturers energy-efficiency data to produce the adjusted spectrum (blue).

Solving this integral for an arbitrary rectangle with width, w, length, l, and height, h, from the arbitrary point (x_0,y_0) gives the relationship shown in Equation 2.4:

$$\begin{aligned}\Omega(x_0,y_0) = &-\arctan\frac{(l-2x_0)(y_0-\frac{l}{2})}{h\times\sqrt{4h^2+l^2+4x_0^2+4(y_0-\frac{w}{2})^2-4l\times x_0}}-\\ &\arctan\frac{(1+2x_0)(y_0-\frac{l}{2})}{h\times\sqrt{4h^2+l^2+4x_0^2+4(y_0-\frac{w}{2})^2+4l\times x_0}}+\\ &\arctan\frac{(1-2x_0)(y_0+\frac{l}{2})}{h\times\sqrt{4h^2+l^2+4x_0^2+4(y_0+\frac{w}{2})^2-4l\times x_0}}+\\ &\arctan\frac{(1+2x_0)(y_0+\frac{l}{2})}{h\times\sqrt{4h^2+l^2+4x_0^2+4(y_0+\frac{w}{2})^2+4l\times x_0}}\end{aligned} \tag{2.4}$$

Using Matlab (The Mathworks, Natick, MA), the relationship in Equation 2.4 was used to develop a model of the solid angle seen at each point on the surface of the ^{241}Am foils. Figure 2-16 shows the model implemented using the geometry of the

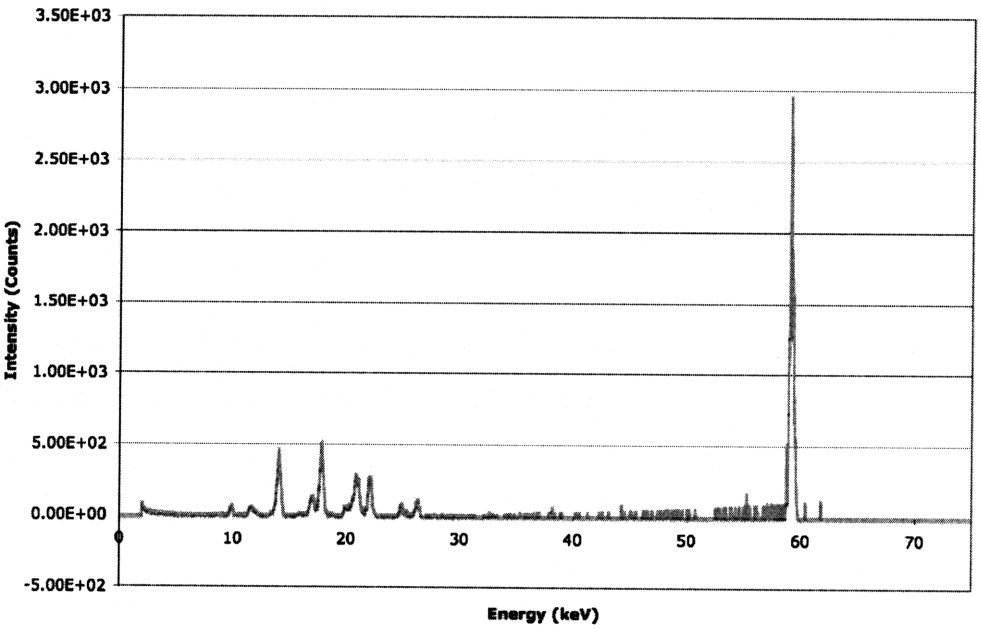

Figure 2-13: Energy spectrum from Dr. Coderre/s ^{241}Am foil (Coderre-4). The spectrum was collected on an Amptek X123 Sn-PIN spectrometer for 90 minutes. The raw counts were corrected using the manufacturer/s energy-efficiency data to produce the adjusted spectrum (blue). While the additional noise is due to the combination of low foil activity and a short measurement time, the underlying energy spectrum of this foil is the same as other foils.

Coderre-1 foil.

There is a 44% variation in the expected dose-rate between the edge of the plate and a position 0.15 inches (3.81 mm) inside the edge while there is only an 11% variation between the position 0.15 inches (3.81 mm) inside the plate and the middle of the foil. Experimental evidence confirms the model/s conclusions. Dosimeters placed on the edge of Dr. Yanch/s 3/32 foil report a dose-rate of 1.150 $\pm$ 0.044 cGy/h. The p-value associated with the measurement of the interior dose-rate (1.234 $\pm$ 0.0325 cGy/h) with two degrees of freedom is less than 0.1. Images of one of Dr. Yanch/s ^{241}Am foils taken previous by An Vu with a BAS Imaging Plates Type MS (FujiFilm, Stamford, CT) indicate that the dose-rate is consistent over the interior surface. One of these images is reproduced in Figure 2-17.

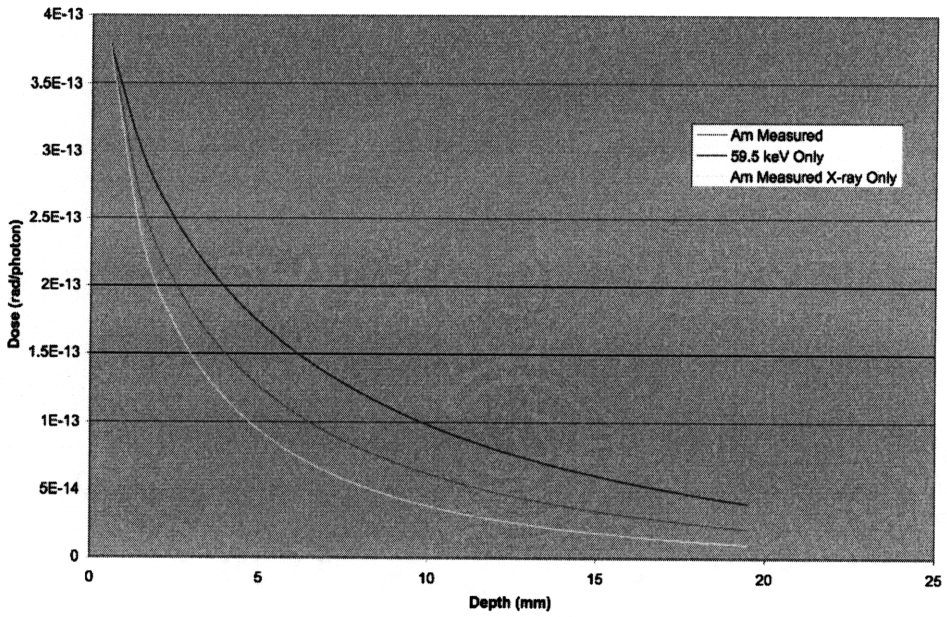

Figure 2-14: The dose per photon deposited at various depths of polyethylene by ^{241}Am 59.5 keV γ-rays, ^{237}Np x-rays and a mixed source of those two radiations all normalized to the same initial dose/photon value as estimated by an MCNP simulation. In the Figure, it is clear that the ^{237}Np x-rays are less penetrating and are preferentially moderated compared to the ^{241}Am γ-rays. The ^{241}Am plate sources are a combination of these two radiations and behave as their weighted average. This Figure was produced and provided by Matthew Davidson.

It is worth noting that the edge effects predicted by the model are relatively modest over most of the surface of the foil (<11% dose-rate variation over 81% of the foil's interior). In general, it was assumed that the interior dose rate was observed evenly across the entire plate. This assumption is strengthened by the fact that, even on the smaller foils, the active growth area of the T25 Falcon flasks used was offset at least a quarter inch from the edges of the foils. Finally, the model was computed using the smallest and most geometrically vulnerable source and should be considered at most a worst-case scenario.

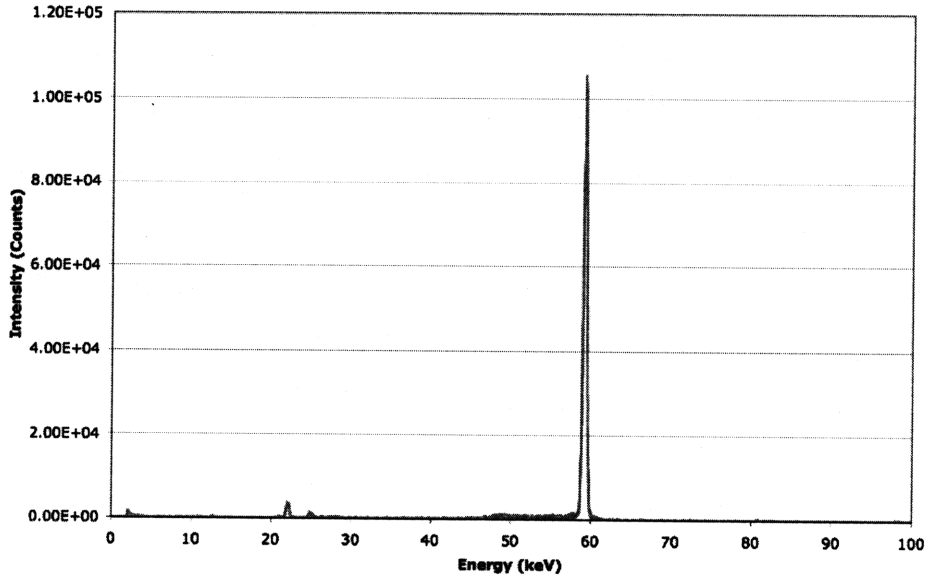

Figure 2-15: The energy spectrum of an ^{241}Am foil from the gold plated side through 0.2 mm of lead shielding. The lead differentially attenuates the low energy ^{237}Np x-rays leaving a field that is dominated by the 59.5 keV γ-ray. This figure is courtesy of Matthew Davidson.

2.2.5 Incubator Arrangement

During any experiment, the Americium foils were arranged into a two-level format: Dr. Yanch/s foils would sit with the gold side facing up on the top level while Dr. Coderre/s foils would be underneath, also with their gold sides facing up. To prevent the higher activity foils from overwhelming the lower dose-rates, the Yanch foils were shielded on their silver sides with 6.35 mm thick lead sheets. Dosimetry data were also collected *in situ* during two experiments to ensure that the dose-rates from the foils inside the incubator matched the dose-rates measured on each foil while in isolation outside the incubator. Figure 2-18 shows the typical arrangement of the foils.

2.2.6 Characteristics of the 250 kVp X-Ray Generator

The Phillips 250 kVp x-ray generator was used to perform acute radiation experiments for comparison with the chronic, low-dose-rate studies. This generator accelerates a current of 15 mA through 250 kV into a 0.4 cm Thoraeus target (0.4

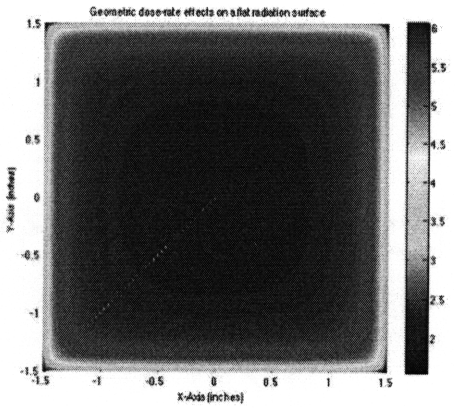

Figure 2-16: Geometric dose-rate effects as seen on the Coderre-1 foil. The cells are modeled to be in a dish approximately $\frac{1}{16}$ of an inch off the surface of the foil. The foil is 3 inches by 3 inches.

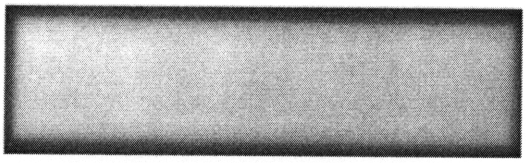

Figure 2-17: Image of one of Dr. Yanch's ^{241}Am foils taken with BAS Imaging Plate by An Vu. The imaging plate has a spatial resolution of 100 μm^2.

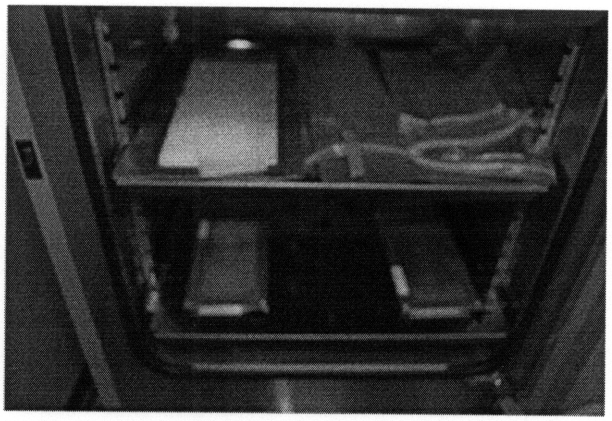

Figure 2-18: Figure depicting the arrangement of the incubator for continuous irradiation experiments. The top shelf holds the higher activity Yanch foils and the smaller, lower activity Coderre foils are on the bottom shelf. The Yanch foils are shielded on their bottoms with 6.35 mm of lead to prevent their radiation from contributing to the dose received by samples on the Coderre foils.

mm of Tin, 0.25 mm of Copper, and 3.35 mm of Aluminum). The x-rays produced by the de-acceleration and ionizations in the target comprise a continuous spectrum with the maximum possible energy being 250 keV and the average photon energy being approximately 83 keV. The accelerator is oriented towards the ground with a stand underneath the target. Raising and lowering the stand results in various dose-rates for the top of the stand. A picture of the setup is shown in Figure 2-19.

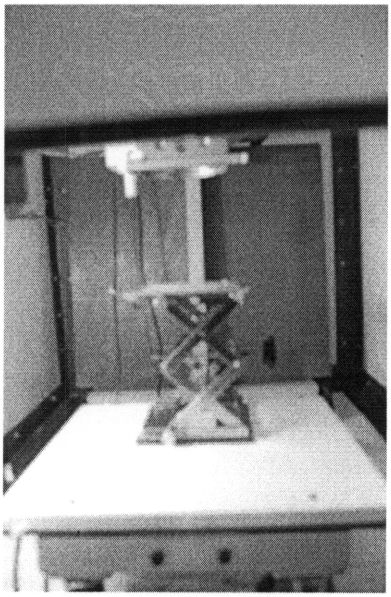

Figure 2-19: A Figure depicting the gun-stand arrangement in the Phillips RT250 irradiation chamber. The gun is oriented toward the ground and the stand is directly underneath. Markings on the table help to properly orient the stand to minimize position induced variance in the dose delivered by the generator. The stand also has marking on its surface to help orient samples properly.

Previous researchers have calibrated the dose-rate as a function of stand height. In particular, Rebecca Raabe found the absorbed dose at a stand height of 11.25 in. was 2.5 Gy/min using a NIST traceable Keithly 617 programmable electrometer [26]. Dr. Coderre also calibrated the dose-rate when the unit was first installed and found a dose-rate of 1.0 Gy/min at a stand height of 9.7 in. No errors were reported for either measurement.

Landauer Dot dosimeters and Luxel Dosimeter badges were also used to calibrate the dose-rate as a function of stand height. The Luxel badge consists of 4 Dot dosimeters, each covered with a different attenuating material. The different shielding conditions enable Landauer software to extrapolate some of the radiation characteristics (type and quality) and estimate a dose received in different parts of the body (both shallow and deep tissue positions, retina, etc.). To best estimate the dose received by a thin layer of cells, the shallow tissue dose was selected as the best estimate. One Luxel badge was used at each stand height, and each badge was irradiated for 5 minutes. The error in the Luxel measurements is estimated from the "counting" statistical error associated with radiation detection (formally, this error is the square root of the number of counts measured).

The Dot dosimeter measurements were carried out in an identical fashion to the personal dosimeter badges except that they were irradiated for 9 minutes with three dosimeters at each position. With multiple dosimeters at each stand height, the error was quantified as the combined inter- and intra-Dot error as defined in Equation 2.2.

The results of those experiments along with the two "Reference" dose-rate points are shown in Figure 2-20. While both the dots and the badges fit a $\frac{1}{r^2}$ curve well (the expected behavior for dose-rate as a function of distance from a point source), there is a troubling discrepancy in the ratio between the Landauer and Reference measurements at 11.25 in. (184.15 mm) and 9.7 in. (223.52 mm) stand height positions. For the Dot dosimeters the ratio between the 11.25 in. measurement and the Reference dose-rate at that height is roughly 6.5 while the ratio between the measurements at a height of 9.7 is approximately 3. For the Luxel badges, the same ratios are 1.5 and 0.9. Given that both the badges and the dots would require an energy dependent calibration for the shift from 80 kVp to a 250 kVp field, the energy spectrum at different heights in the chamber is more or less constant (attenuation through the air is thought to be slight and ignored), and the ratio between any two points from one measurement system to another should be constant over distance. Given the

unknown efficiency of the Landauer equipment in the 250 kVp field and the NIST traceable equipment used to generate the 2.5 Gy/min measurement, the experiments were conducted using the 2.5 Gy/min reference dose-rate point only. Discovering the source of the discrepancy between the OSL dosimeters and the ion chamber is the subject of future work. Finally, it is important to note that many of the conclusions discussed later do not rest on a tight calibration of the x-ray machine. It is generally sufficient for most conclusions that the x-ray machine is delivering orders of magnitude higher dose-rates.

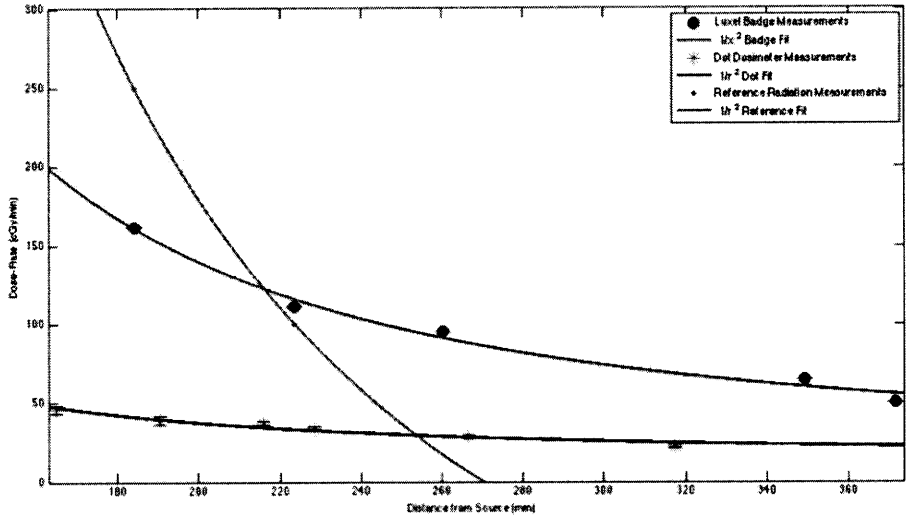

Figure 2-20: Dose-Rate as a function of distance as measured by Landauer Dot Dosimeters, Luxel personal dosimeter badges and by previous researchers. All measurements were conducted in a 250 kVp field at 15 mA and into a 0.4 Th target (except the 100 cGy/min Reference point which had a current of 12 mA). The μStar Dots were exposed for 9 minutes while the Luxel badges were exposed for 5 minutes each. Both the badges and the dots have different ratios between their measurements at the 11.25 in. and 9.7 in. stand height positions and the reference dose-rates given at those points. Both the dots and the badges have good fits to a $\frac{1}{r^2}$ curve: $R^2_{dot} = .952$ and $R^2_{badge} = .987$.

Chapter 3

Biological Protocols

This section describes the techniques and materials used to maintain the AA8 and EM9 cell lines and the protocols used to explore their growth rate and clonogenic survival under acute and chronic radiation conditions.

3.1 Cell Handling and Maintenance

3.1.1 Medium Preparation

Both EM9 and AA8 cell lines were maintained using the guidelines reported by K. Skov *et al.* [32]. The cells were cultured in medium composed of Dulbeccos Modified Eagles Medium with 4,500 mg/L glucose and without sodium pyruvate, supplied by either Hyclone (Waltham, MA) or Cellgro (Manassas, VA) as available from Van Waters and Rogers (VWR), 10% Hyclone fetal calf serum (Waltham, MA), and 1% 10,000 units/ml penicillin-streptomycin from Cellgro (Manassas, VA). Before use, the mixed medium was filtered through a 0.2 μm filter (Nalgene, Waltham, MA) into a sterile receiver flask. During any one experiment the cells were fed from a single lot of prepared medium to prevent inconsistencies in the preparation of the medium from influencing the assays' outcomes. The cells were grown in VWR International (Bridgeport, NJ) incubators in humid conditions at 37°C and 5.0% CO_2.

3.1.2 Cell Passaging

Both cells lines were subcultured using the following protocol. The cells were subcultured every 2-6 days over the course of the experiment. T175 Falcon stock flasks (San Jose, CA) were inspected under a light microscope to roughly ascertain the level of confluence in the flask. Following inspection, the flasks were washed in 15 ml of sterile DPBS without Calcium and Magnesium (Hyclone, Waltham, MA). If the flask had grown over confluent with dead cells floating in the medium, the flasks were washed twice with 15 ml of DPBS. 1 ml of 0.05% Trypsin-EDTA (Cellgro, Manassas, VA) dissolved in HBSS without Calcium, Magnesium, or Sodium Bicarbonate was added to each flask. The flask was rocked to wash the surface evenly with the Trypsin and stored in the 37°C incubator for approximately 3 minutes. Following incubation, the flasks were shaken and inspected under a light microscope to confirm that cells had rounded and detached. The flasks were washed with 10 ml of medium repeatedly and the total volume collected in 15 ml Falcon tubes (San Jose, CA). The solution was well mixed with the pipetter and the density was counted using either a hemocytometer or a Z2 Beckman-Coulter Coulter Counter (Fullerton, CA). The cells were re-plated so as to give a 1:10 subculturing ratio (for a confluent flask) into new T175 flasks. The final volume of cells and medium was approximately 20 ml. Once the cells reached 20 passages, they were discarded and a new line was thawed from frozen stocks.

3.2 Biological Assays

3.2.1 Clonagenic Survival Assay

AA8 and EM9 cells from an exponential phase stock solution were harvested as outlined above. The density of the harvested solution was determined using the Z2 Coulter Counter and serially diluted in fresh medium to provide a plating density of 100 cells / ml. To prevent irregular dilutions, mixing at each step with a pipetter was undertaken vigorously. 4 ml from this dilute solution were aliquoted into T25 Falcon flasks (San Jose, CA) with 0.2 μm filtered caps. The final plating density was 400 cell

/ 25 cm^2. After plating, these flasks were allowed to sit in the incubator for at least 4 hours and no more than 8 hours to allow for the cells to attach to the polystyrene surface.

After sitting, the flasks were either placed on the gold side of the ^{241}Americium foils (NRD, Grand Island, NY) or irradiated in the Phillips RT250 X-ray machine (Bothell,WA). For continuous irradiation studies, the desire to irradiate AA8 and EM9 cells lines simultaneously and the limited space available on some of the smaller foils limited the number of flasks per cells line to 2 on any given Americium foil (with the exception of the Coderre-1 foil which can only accommodate a single flask at a time). The continuous dose-rates investigated were: 1.23 ± 0.0325 cGy/h (Yanch Foil), $4.86 \pm .540 \times 10^{-1}$ cGy/h (Coderre-1), $9.08 \pm .390 \times 10^{-3}$ cGy/h (Coderre-2), $3.30 \pm .800 \times 10^{-3}$ cGy/h (Coderre-3), and $1.99 \pm .610 \times 10^{-3}$ cGy/h (Coderre-4) as detailed in Table 2.3. For the EM9 line, an additional radiologic condition, created by shielding a Yanch foil with 0.8 mm of lead, was used to explore the RBE effects between a primarily γ-ray source and primarily x-ray source. The control flasks for the continuous experiments were stored in a separate incubator without radiation to serve as a negative control.

The cells were irradiated at 0.2, 0.5, 1, 2, 5, and 10 Gy at 2.5 Gy/min in the Phillips RT250 x-ray generator. The acute studies had separate controls that were sham irradiated in order to capture any possible toxic effect associated with the time spent outside the incubator during dosing. After dosing, the flasks were placed in the same incubator as the continuous control flasks so as to avoid additional inadvertent irradiation.

At the conclusion of 7 days, the flasks were removed from their incubators, had their medium aspirated, and liberally washed twice with PBS. After washing, the flasks were stained with 2 ml of 0.5% crystal violet in 6.0% glutaldyhde in water. After staining for about 25 minutes, the plates were washed thoroughly in water and set to dry. Only flasks with distinct, unmerged colonies were counted. Only colonies above

50 cells per colony were considered viable and scored. The colonies were counted by eye (a 50 cell colony found under a light microscope served as a standard) using a colony-counting pen for accuracy.

3.2.2 CyQUANT Growth Assay

AA8 and EM9 cells were harvested from a 70-90% confluent stock flask as outlined above. The density of the harvested solutions were measured using a Z2 Beckman-Coulter Coulter Counter (Fullerton, CA), and serial dilutions were prepared with fresh medium to provide densities of 400, 4000, 40000 and 400000 cells per 200 μl of solution. The cells were kept on ice during the preparation of the dilutions. After the dilutions were prepared, 400 μl of the various solutions were plated into five Falcon 96-well plates (San Jose, CA) using a multi-channel pipetter. Each density (400 cells / well, 4000 cells / well, 40000 cells / well, and 400000 cells / well) of each line was plated into 6 wells on each plate of the 5 plates.

After 8 hours, the cells were placed on the radiative foils. The dose-rates explored were: 1.23 ± 0.0325 cGy/h (Yanch Foil), $9.08 \pm .390 \times 10^{-3}$ cGy/h (Coderre-2), $3.30 \pm .800 \times 10^{-3}$ cGy/h (Coderre-3), and $1.99 \pm .610 \times 10^{-3}$ cGy/h (Coderre-4). Coderre-1 was unusable since the foil area is smaller than the area of a 96 well plate. In addition to the irradiated plates, the 5th 96-well plate was used as a negative control and stored in a separate incubator to avoid inadvertent exposure.

After 4.5 days, the 96-well plates were collected and stained using the CyQUANT protocol provided by Invitrogen (Carlsbad, California) [17]. Under a light microscope, the various densities were checked to determine which wells were within the linear response region of the assay *i.e.*, which densities had fewer than 20,000 cells per well. The initial density check under the microscope was checked against a coulter counter reading from one of the wells at that particular density to ensure that the cells were within the linear range. It was found that only the 200 cells per 200 μl wells were comfortably within the margin and only these wells were stained.

The wells were first gently drained of medium by inversion of the plates. 100 μl of CyQUANT dye solution (a stock solution of this dye solution was prepared from 22 μl of CyQUANT reagent with 2.2 ml of HBSS buffer in 8.8 ml of DI water) were added to each well by a multi-channel pipetter. The plates were then incubated at 37°C for 30 minutes. After the incubation period, the plates were wrapped in aluminum foil and transported to Dr. Bevin Engelward/s lab. A microplate reader then read the plates with an excitation frequency of roughly 485 nm and detection frequency of approximately 530 nm.

Chapter 4

Results And Discussion

This chapter presents the results of the clonogenic and CyQUANT experiments. From these data, conclusions about the effect of chronic radiation and the relative importance of the XRCC1 protein will be made. Specifically, the discussion section will provide an analysis of the results in the context of the trends and findings in the published literature described in the first chapter. The chapter will conclude will a look forward to possible future work.

4.1 Results

4.1.1 Clonogenic Assay: Continuous and Acute

Table 4.2 summaries the clonogenic assay data for both AA8 and EM9 under continuous and acute irradiation schemes while Figure 4-1 presents a representative picture of a stained experimental flask. The acute and continuous data are plotted separately in Figures 4-2 and 4-3. A linear-quadratic model of the form $y(D) = e^{-\alpha D - \beta D^2}$ and a "Multi-Target Single Hit" model of the form $y(D) = 1 - (1 - e^{\frac{D}{D_0}})^n$ model were used to fit the acute data. The parameters for each model, α and β, D_0 and n, are summarized for both cell lines in Table 4.1. Each model also includes a R^2 as a figure of merit for the model's predictive ability. These two models are reducible to each other in the form: $y(D) = e^{\frac{-D}{D_0}}$ where D_0 is $\frac{1}{\alpha}$.

Table 4.1: Parameters describing the Linear-Quadratic and Multi-Target Single Hit Models for both cells lines. Despite having different forms, the models' parameters reduce the two models into a single function of the form: $y(D) = e^{\frac{-D}{D_0}}$. R^2 is used to determine how well the models parameters fit the particular data.

Cell Line	α	β	LQ R^2	D_0	n	MTSH R^2
AA8	0.5656	0	0.8941	1.768	1	0.8941
EM9	1.498	0	0.9144	0.667	1	0.9144

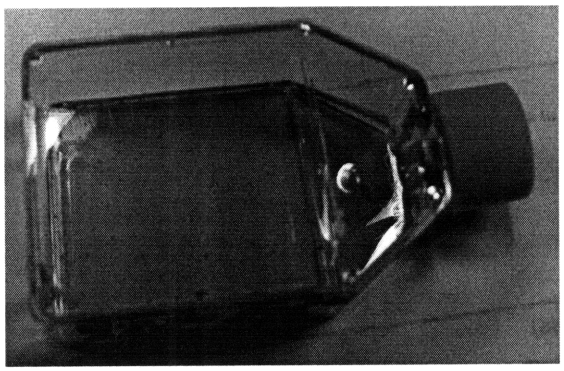

Figure 4-1: A picture of a flask whose colonies are representative of the distribution of colony sizes found on both the AA8 and EM9 clonogenic flasks. While visible to the eye, the largest colonies were often only tenths of a millimeter in diameter. The smaller colonies, which were considerably smaller, had to be compared to a standard sized colony that was counted under a light microscope and found to have approximately 50 cells. The colonies ranged in size, with some of the largest colonies being around 0.1 mm in diameter.

Table 4.2: Summary of data from continuous and acute clonogenic assays. The colony-forming fraction was computed by dividing the average number of colonies observed at a particular dose or dose- rate by the average number of colonies formed in that particular exposure regime. The individual errors associated with any one condition (as represented by the standard deviation of measurements in that set) were propagated to give the error to the colony-forming fraction. Conditions in bold represent an RBE dose-rate achieved by shielding a Yanch foil with 0.8 mm of lead.

Dose-Rate (cGy/h)	Dose (Gy)	Number of AA8 Colonies in Flask #1	Number of AA8 Colonies in Flask #2	Standard Deviation of AAB Pairs	AA8 Colony Forming Fraction (%)	Error in AA8 Colony Fraction (%)	Number of EM9 Colonies in Flask #1	Number of EM9 Colonies in Flask #2	Standard Deviation of EM9 Pairs	EM9 Colony Forming Fraction (%)	Error in EM9 Colony Forming Fraction (%)
Continuous Exposure											
0.00E+00	0.00E+00	389	364	1.77E+01	1.00E+00	6.64E-02	299	320	1.48E+01	1.00E+00	6.79E-02
1.99E-03	3.34E-03	314	351	2.62E+01	8.83E-01	9.16E-02	101	130	2.05E+01	3.73E-01	1.84E-01
3.30E-03	5.54E-03	304	314	7.07E+00	8.21E-01	5.22E-02 57	58	7.07E-01	1.86E-01	4.95E-02	
6.89E-03	1.16E-02	No Result	No Result	No Result	No Result	No Result	105	80	1.77E+01	2.99E-01	1.97E-01
9.08E-03	1.53E-02	282	259	1.63E+01	7.18E-01	7.63E-02	60	35	1.77E+01	1.53E-01	3.75E-01
4.86E-01	8.16E-01	No Result	No Result	No Result	No Result	No Result	48	No Result	No Result	1.55E-01	
1.23E+00	2.07E+00	265	330	4.60E+01	7.90E-01	1.61E-01	19	30	7.78E+00	7.92E-02	3.21E-01
Acute Exposure											
0.00E+00	0.00E+00	405	No Result	No Result	1.00E+00	No Result	299	No Result	No Result	1.00E+00	No Result
1.50E+04	2.00E-02	446	No Result	No Result	1.10E+00	No Result	249	No Result	No Result	8.33E-01	No Result
1.50E+04	1.00E-01	270	No Result	No Result	6.67E-01	No Result	218	No Result	No Result	7.29E-01	No Result
1.50E+04	5.00E-01	300	No Result	No Result	7.41E-01	No Result	157	No Result	No Result	5.25E-01	No Result
1.50E+04	1.00E+00	246	No Result	No Result	6.07E-01	No Result	69	No Result	No Result	2.31E-01	No Result
1.50E+04	5.00E+00	33	No Result	No Result	8.15E-02	No Result	6	No Result	No Result	2.01E-02	No Result
1.50E+04	1.00E+01	2	No Result	No Result	4.94E-03	No Result	0	No Result	No Result	0.00E+00	No Result

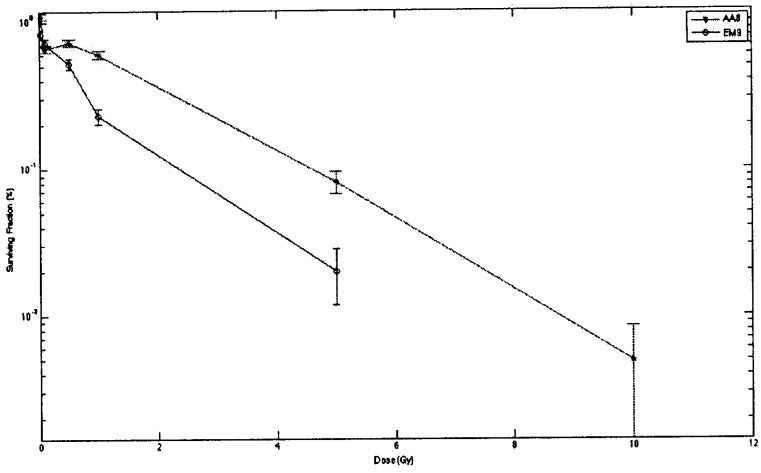

Figure 4-2: Colony forming assay results for AA8 (red) and EM9 (blue) cells exposed acutely to a 250 kVp x-ray field and allowed to grow for 7 days. The x-ray dose-rate was 2.5 Gy/min with doses between 0.02 Gy and 10 Gy as reported in Table 4.2. The survival data were fit with both a "multi-target single hit" (MTSH) model and a "linear-quadratic" model. For the linear-quadratic model, the AA8 cell lines $\alpha = 0.5656$, $\beta = 0$, and the goodness of fit, as assessed by R^2, was 0.8941. The parameters for the EM9 fit are: $\alpha = 1.498$, $\beta = 0$, and $R^2 = .9144$. For the MTSH model, the parameters for the AA8 fit are: $n = 1$, $D_0 = 1.768$ and $R^2 = 0.8941$. The parameters for the EM9 fit are: $n = 1$, $D_0 = 0.6675$, and $R^2 = .9144$. These two models are reducible to each other in the form: $y(D) = e^{\frac{-D}{D_0}}$ where D_0 is $\frac{1}{\alpha}$. The error bars are calculated based on the Poisson "counting" error associated with random processes.

A hypothesis-testing matrix using a Students T-test is reported in Table 4.3 assessing the significance of the colony forming fractions (CFFs) of AA8s and EM9s at the same continuous dose-rate and the significance of the CFFs of either AA8s or EM9s to other AA8s or EM9s at different continuous dose-rates. Generally, the continuous exposure results indicate a suggestive (p-values between <0.05 and <0.20) difference between all irradiated dose-rates CFFs and the unirradiated controls for EM9s and AA8s as well as a suggestive (p-values between <0.05 and <0.20) difference between the CFFs of AA8s and EM9s at any particular dose-rate. Typically, there is not a significant difference between the CFFs of either AA8s or EM9s at a given dose-rate to AA8s or EM9s at another dose-rate.

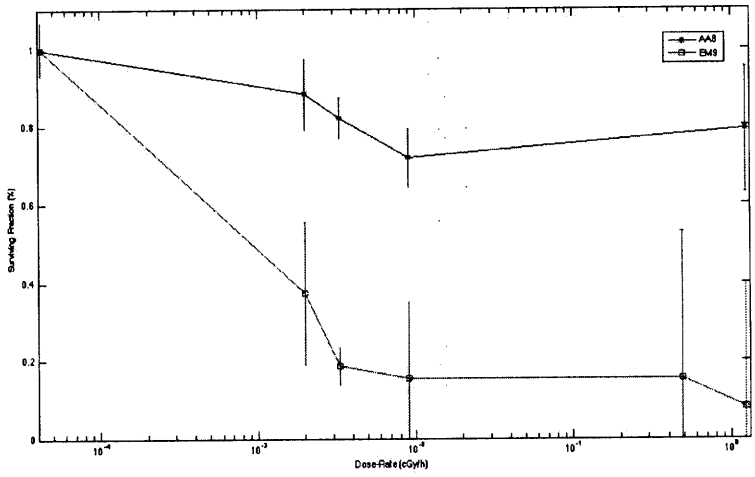

Figure 4-3: Colony forming assay results for AA8 and EM9 cells exposed chronically to low-dose-rate radiation from ^{241}Am sources for 7 days. The dose-rates, as reported in Table 4.2, range from 0.00199 ± 0.00061 cGy/h to 1.23 ± 0.03 cGy/h. There is a pronounced difference between the survival of the AA8 and EM9 pairs at all dose-rates. There is also a lack of conclusive dose-rate structure to both curves as seen by the hypothesis testing reported in Table 4.3. The error bars represent the error derived from a technical repeat at each dose-rate (except on the 9.08 ± .390 × 10^{-3} cGy/h (Coderre-2) foil in which case no error bars are indicated).

Table 4.4 compares the relative CFF difference between AA8s and EM9s under acute conditions to the same difference under chronic irradiation conditions for a given dose using a Students T-test. Only the lowest three dose-rates were used for the comparison because the models derived for the acute data only behave well at low doses. At all low doses, a Students T-test for paired data indicates there is a suggestive (p-values range from <0.05 to <0.20) difference in the differential responses of the two irradiation conditions (acute and chronic). At all doses, the difference between AA8 and EM9 CFFs increases with decreasing dose-rate. The table also compares the significance of the CFF difference between acute and chronic cases for a given cell line at a particular dose. For both EM9s and AA8s, there are significant differences between the chronic and acute CFFs with the chronic cases uniformly having smaller CFFs.

Table 4.3: A matrix with the T-values from various intra-cell line comparisons and intra-dose-rate comparisons for the continuous exposure Colony Forming Fraction (CFF) data from Students T-test. The diagonal line compares the AA8 and EM9 fractions at a particular dose-rate. The lower half of the matrix compares a particular EM9 dose-rate to other EM9 dose-rates. The top half of the matrix compares a particular AA8 dose-rate to the other AA8 dose-rates. The p-values for 0.05, 0.10, 0.15, and 0.20 for two degrees of freedom are 2.920, 1.886, 1.386, and 1.061. The dose-rate in bold indicates that the dose-rate was achieved by shielding a Yanch Foil with 0.8 mm of lead and has a 59.5 keV γ-ray dominated energy profile. These T-values indicate that there are significant differences between the control and irradiated population's CFF values for both AA8 and EM9 lines. They also indicate that there are significant differences between the CFF values between AA8 and EM9 lines for any particular dose-rate. However, there do not generally appear to be any significant CFF differences between different dose-rates inside the same cell line.

		AA8-AA8						
	Dose Rate (cGy/h)	1.23E+00	4.86E-01	9.08E-03	**6.89E-03**	3.30E-03	1.99E-03	0.00E+00
EM9-EM9	1.23E+00	1.98E+00	No Result	4.04E-01	No Result	1.83E-01	5.02E-01	1.21E+00
	4.86E-01	2.36E-01	No Result	No Result	No Result	No Result	No Result	No Result
	9.08E-03	1.50E-01	5.33E-03	1.48E+00	No Result	1.11E+00	1.38E+00	2.79E+00
	6.89E-03	5.87E-01	7.31E-01	3.45E-01	No Result	No Result	No Result	No Result
	3.30E-03	3.29E-01	6.26E-01	8.72E-02	5.56E-01	8.83E+00	5.88E-01	2.12E+00
	1.99E-03	7.94E-01	1.18E+00	5.27E-01	2.75E-01	9.81E-01	2.48E+00	1.03E+00
	0.00E+00	2.81E+00	1.24E+01	2.22E+00	3.36E+00	9.69E+00	3.20E+00	2.90E+00

Table 4.4: A table comparing the significance of the differential AA8-EM9 colony forming fraction (CFF) between the continuous and acute exposures for a given dose and the significance of the difference between exposure regimes at any given point for either AA8s or EM9s. Based on models derived for the acute survival data, CFF fractions for the AA8 and EM9 lines were extrapolated for the lowest three dose-rates since the model behaves well in this region. The error associated with these values scales with the goodness of fit metric, R^2. The differences between AA8 and EM9 CFF were then compared across exposure modalities and used to generate a T-value for a paired data ("AA8-EM9 Differential Difference T-Value"). The differences between the CFFs of the two exposure modalities for any one cells line at a particular dose were also tested for both EM9s and AA8s ("Chronic-Acute Difference T-Value"). The p-values for one degree of freedom for 0.05, 0.10, 0.15, and 0.20 are 6.314, 3.078, 1.936, and 1.376. These T-values indicate that there is a significant enhancement of the AA8-EM9 CFF difference between exposure modalities at all dose-rates and a significant difference for the CFFs of AA8s and EM9s between the chronic and acute exposures.

Dose (Gy)	AA8-MHST CFF (%)	AA8-MHST Error (%)	EM9-MHST CFF (%)	EM9-MHST Error (%)	AA8-EM9 Differential Difference T-Value	AA8 Chronic-Acute Difference T-Value	EM9 Chronic-Acute Difference T-Value
0.0153	0.991	0.0849	0.977	0.0837	1.37	2.39	2.14
0.00554	0.997	0.0853	0.992	0.0849	4.49	1.76	8.20
0.00334	0.998	0.0854	0.995	0.0852	2.13	0.918E	3.07

Table 4.5: A table summarizing the results of the CyQUANT growth assay for AA8s and EM9s under various dose-rates. The table reports the number of cells after 4.5 days from an intial plating of 200 cells / well. The errors in the measurements are calculated by the standard deviation of the group of wells in that particular dose-rate.

Dose-Rate (cGy/h)	.000E+00	1.99E-03	2.20E-.03	9.08E-03	1.23E+00
	AA8				
6*Well Populations (Number of Cells)	1561.586	727.861	442.764	555.629	1076.111
	1861.836	1175.28	1089.855	1353.093	1638.073
	2223.297	1220.945	853.069	1042.725	1007.0770
	1844.299	1043.712	1678.217	1539.359	1627.261
	2365.629	1276.078	1023.722	764.56	361.585
	No Result	No Result	1583.205	1669.473	991.935
Average	1971.3294	1088.7752	1111.805333	1154.139833	1117.007
Error	322.0927766	219.2738169	461.7014422	441.8020758	475.800675
	EM9				
6*Well Populations (Number of Cells)	No Result	443.441	623.367	550.407	681.963
	671.018	368.293	378.017	361.227	435.296
	690.962	631.724	526.166	629.823	665.416
	650.942	263.986	337.066	399.941	395.312
	788.131	639.616	425.474	858.94	606.571
	919.275	422.778	330.18	279.055	339.82
Average	744.0656	461.6396667	436.7116667	513.2321667	520.7296667
Error	111.2070618	148.476428	116.3545402	212.2586635	148.3616307

4.1.2 CyQUANT Assay

The data from the continuous exposure CyQUANT assay are reported in Table 4.5. The average number of cells after 4.5 days and associated errors are plotted against their radiological conditions in Figure 4-4. The error bars are from the pooled error of five technical repeats at each dose-rate for each cell line. A hypothesis-testing matrix using a Students T-test is reported in Table 4.6. Similar to Table 4.3, the matrix tests the significance of the growth rates of AA8s and EM9s at a particular dose-rate and the significance of either AA8s or EM9s to other AA8s or EM9 cells at two different dose-rates. In order to control for any possible errors in initial plating and the natural differential in growth rate between AA8s and EM9s, the comparisons between the two lines at various dose-rates (*i.e.* the diagonal values in the matrix) are normalized by the growth rate in their respective negative controls. In general, there are significant ($p<0.05$) differences between the control, unirradiated growth rate and the growth rates for both AA8 and EM9 lines under any radiological stress. There do not appear to be significant differences between the growth rates for the various dose-rates for either AA8s or EM9s or significant differences between the growth rates of AA8s and EM9s under the same radiological conditions.

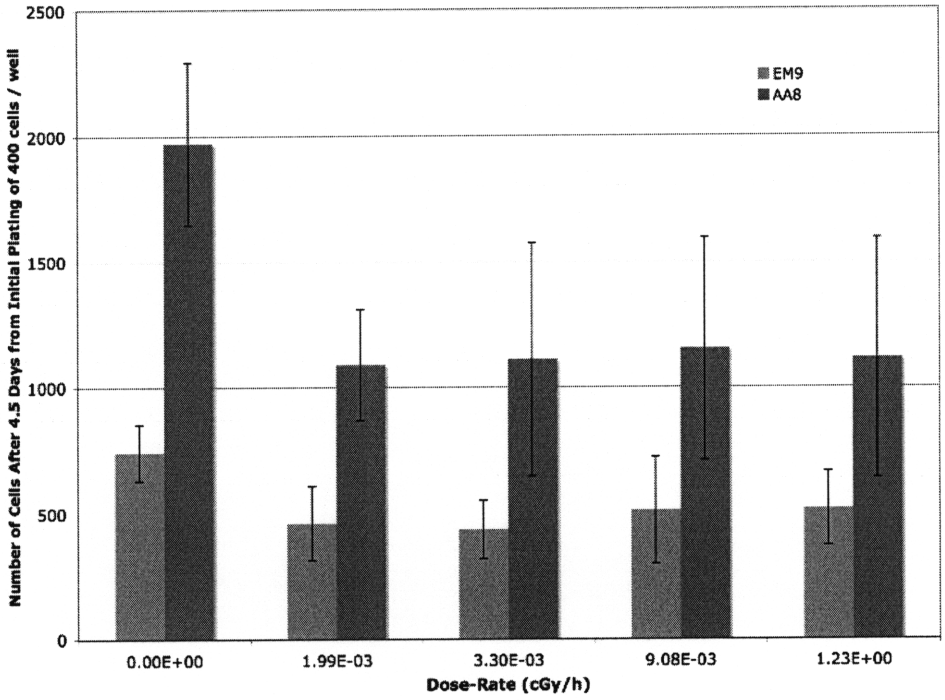

Figure 4-4: A bar chart summarizing the average number of AA8 and EM9 cells in at least five wells at each dose-rate after 4.5 days. The error bars are based on the pooled error from 5 technical repeats. Each well was initially plated at a density of 400 cells / well. While there is a significant difference (see Table 4.6) between irradiated and non irradiated samples for each cell line, the inter-cell line differences and cell line differences at any particular dose-rate are not significant.

4.2 Discussion

Generally, the results indicate that low-dose-rate radiation has significant effects on the clonogenic survival and growth rate of the AA8 and EM9 cells lines. Moreover, the results highlight some interesting modulation of the importance of the XRCC1 mutation to clonogenic survival as a function of dose-rate.

Specifically, the results indicate a significant or suggestive decrease in both clonogenic survival and growth rate for irradiated flasks as compared to non-irradiated samples for both AA8 and EM9 cell lines as seen in Tables 4.6 and 4.3. There are also significant differences between the clonogenic survival of the AA8s and EM9s under all the chronic dose-rates explored with the EM9 line being more susceptible to

Table 4.6: A matrix with the T-values from various intra-cell line comparisons and intra-dose-rate comparisons for the continuous exposure CyQUANT data from Students T-test. The diagonal line compares AA8 growth behavior to EM9 growth behavior normalized by the negative control for the same dose-rate. The lower half of the matrix compares a particular EM9 dose-rate to other EM9 dose-rates. The top half of the matrix compares a particular AA8 dose-rate to the other AA8 dose-rates. The p-values for 0.05, 0.10, 0.15, and 0.20 for two degrees of freedom are 1.860, 1.397, 1.108, and 0.889. These values indicate that the radiation significantly changes the normal growth rate of each particular cell line, but there are no significant differences among the growth rates of irradiated cells both in lines and in dose-rates in a single line.

		AA8-AA8				
	Dose Rate (cGy/h)	0.00E+00	1.99E-03	3.30E-03	9.08E-03	1.23E+00
2*	0.00E+00	5.69E+00	3.58E+00	2.41E+00	2.36E+00	2.35E+00
	1.99E-03	2.41E+00	2.45E-01	7.11E-02	2.09E-01	8.51E-02
EM9-	3.30E-03	3.02E+00	2.09E-01	5.69E-02	1.05E-01	1.24E-02
EM9	9.08E-03	1.52E+00	3.15E-01	5.00E-01	2.80E-01	9.03E-02
	1.23E+00	1.90E+00	4.45E-01	7.04E-01	4.58E-02	3.03E-01

the killing effects of radiation. Most interestingly, the difference between the clonogenic survival of the pair of lines appears to be inversely modulated by the exposure regime with the chronic irradiation accentuating the difference between the mutant and wild type phenotypes. That is, XRCC1 mutants appear to have a highened sensitivity under low-dose-rate, chronic conditions as opposed to their sensitivity at high dose, high dose-rate, acute exposures.

Unfortunately, there are some reasons to be cautious about the inverse dose-rate effect observed with respect to the relative importance of the XRCC1 protein. While continuous low-dose-rate studies of CHO cells are relatively new, many labs have conducted acute exposure studies. Indeed, in characterizing the newly isolated mutants, Thompson *et al.* exposed both lines to 40 kVp x-rays at dose-rates between 2.2-4 Gy/min with doses ranging from 0 Gy to approximately 11 Gy. Their results, shown in Figure 4-5, found the D_0 dose for AA8s and EM9s to be 1.2 Gy and 0.6 Gy with an extrapolation number, n, for both around 100 [35]. The D_0 values measured in this experiment agree with Thompsons results. The D_0 for EM9s cells was 0.668 Gy, and

the D_0 for AA8s was 1.768 Gy with a 95% confidence interval of [0.312 Gy, 3.23 Gy]. There is, however, considerable disagreement between the Thompson extrapolation number ($\approx$ 100) and the value measured in this work ($\approx$ 1). As seen in a comparison of Figure 4-2 and Figure 4-5, this disagreement between parameters influences the shape (or presence) of a repair shoulder at low doses for both AA8s and EM9s. Repair shoulders are prominent features in all other acute clonogenic survival studies done on AA8 and EM9 cell lines with x-rays including work done by Skov *et al.* [32] and Green *et al.* [2].

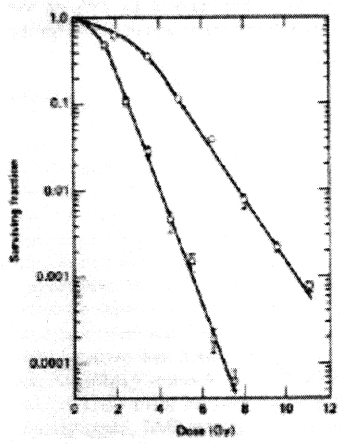

Figure 4-5: Clonogenic survival curve for AA8 and EM9 cell lines exposed acutely to 40 kVp x-rays at a dose-rate between 2.2-4 Gy/min. The (D_0, n) for the AA8s and EM9s lines are (1.2, 100) and (0.6, 100) respectively. For both cell lines, a repair shoulder is prominent at the low end of the Dose axis. [35].

The structure of the curves for AA8s and EM9s in Figure 4-2 mimics the result expected from cells irradiated with high LET radiation (i.e. α particles, protons, low energy electrons, etc.) or the result expected from cells irradiated at very high dose-rates [37]. With high LET radiation, the increased density of energy deposition makes DNA repair more difficult (if not impossible) when cells are critically struck thus, decreasing the relative importance of DNA repair mechanisms. Similarly, the overwhelming effect of high dose-rate radiation makes repair mechanisms less important. These possible explanations are excluded by the fact that one of the cited studies showing repair shoulders for both AA8s and EM9s used a much lower energy

(higher LET) x-ray field than the one used in this study (40 kVp field versus 250 kVp field) with a comparable dose-rate (2.5 Gy/min versus 2.2-4 Gy/min) [35]. Since the radiation quality or dose-rate is unlikely to be the source of the repair shoulder discrepancy, the difference must lie in some other procedural discrepancy.

One common difference between studies reporting a repair shoulder and this work is the temperature conditions during irradiation. All of the studies showing repair shoulders kept their cells on ice while outside of the incubator [35, 2, 32]. A study by vanAnkeren *et al.*, examining the effect of temperature on SSB repair in AA8s and EM9s, found that increased temperatures increased the rate of DNA repair, but under incubator condition (i.e. under 5.0% CO_2) [39]. Perhaps outside the incubator, the increased temperature has the effect of suppressing rather than priming the activity of the cells DNA repair mechanisms. Low temperatures outside the incubator might also shield the cells from harmful effects related to a medium pH change associated with the lack of sufficient CO_2 in the atmosphere (a pH change during the acute exposure protocol was noted by a distinct shift in the medium color from pink to purple). Since an acute exposure experiment did involve the flasks spending between 25-45 minutes outside the incubator, temperature/pH effects are a potential explanation for the lack of repair activity seen in this work.

Nevertheless, despite the repair shoulder discrepancy, none of the acute studies cited indicate that the difference in AA8 and EM9 clonogenic survival would be sufficient at very low doses to overcome the dramatic difference in clonogenic survival seen in Figure 4-3 [35, 2, 32]. It seems reasonable to assume that despite possible procedural errors in the acute assay, there is a genuine inverse dose-rate effect with respect to the importance of the XRCC1 mutation in recovery from ionizing radiation.

Future work will have to be done to elucidate the connection between the biological function of XRCC1 and this particular trend in the radiosensitivities of EM9s and AA8s. Previous works have noted that EM9s are repair deficient and not repair incapable indicating that the XRCC1 mutation may be affecting the efficiency but

not the capacity for base excision repair [39]. This observation fit well with the finding that XRCC1 has been associated with a complex of proteins including DNA ligase III, polymerase β, and poly (ADP-ribose) polymerase [40], and XRCC1 may function as a scaffolding protein, coordinating the structure of this protein complex of polymerases and ligases [24]. However, this coordination role would seemingly imply a more traditional dose-rate response since decreasing dose-rate would relieve the pressure on any inefficiency presented by a lack of coordination.

Future clonogenic survival studies should include a parallel BrDU (or an equivalent) assay to give information about the cell cycle distributions of the irradiated and control AA8 and EM9 flasks. While the CyQUANT assay is very useful for counting the number of cells present with intact DNA, it isnt particularly helpful at discriminating between fully functioning cells and living cells that have entered a state of growth arrest or are otherwise mitotically inactive since its dye only binds intact nuclear DNA [17]. With a BrDU assay, the experimental setup could be used to probe whether the inverse dose-rate effect is the result of cellular arrest in a sensitive cell cycle phase, or by contrast, whether the effect is the result of dose-rates sufficiently underneath the endogenous rate of DNA damage that the damage goes unnoticed. This cell cycle information would help resolve the conflicting explanations of the inverse dose-rate effects advanced by Mitchell (cell cycle arrest) [23] and Vilenchik and Knudson (unnoticed damage) [41].

The inverse dose-rate effect noted above, and generally, the significant difference seen between chronically low-dose-rate irradiated samples and their negative controls also beg the question of the location and/or existence of a sublimiting dose-rate. Future studies should probe the lower bound for dose-rate, beneath which no significant differences in clonogenic survival or growth rate are observed between control and irradiated samples. Alternatively, a search for the sublimiting dose-rate may confirm the parabolic killing curve shape advanced by Vilenchik and Knudson and reproduced in Figure 1-2 if no sublimiting dose-rate is found. This study is possible using the

current sources shielded by some material (aluminum or lead).

While in pursuit of the sublimiting dose-rate, it will be possible to investigate, in parallel, the relative biological effect (RBE) associated with transitioning from a low energy (10-30 keV), ^{237}Np x-ray dominated dose to a higher energy (59.5 keV) ^{241}Am γ-ray dominated dose. While the preliminary results in Table 4.2 are not statistically significant and dose-rate effects are not being strictly controlled for, the higher clonogenic survival from the filtered 6.89×10^{-3} cGy/h source compared to the 3.30×10^{-3} cGy/h unfiltered source hints at the relative importance of the higher LET ^{237}Np x-rays. Future studies should demonstrate this importance more rigorously.

Bibliography

[1] L. Bonnet H. Planel C. Caratero A. Caratero, M. Courtade. Effect of a continuous gamma irradiation at a very low dose on the life span of mice. *Gerontology*, 44:272–276, 1998.

[2] P.M. Stoudt A. Green, A. Prager and D. Murray. Relationships between dna damage and the survival of radiosensitive mutant chinese hamster cell lines exposed to γ irradiation. part 1: Intrinsic radiosensitivity. *Int. J. Radiat. Biol.*, 61(4), 1992.

[3] Lucas A.C. Polf J.C. Akselrod, M.S. and S.W.S. McKeever. Optically stimulated luminescence of al_2o_3. *Radiation Measurements*, 29(3-4):391–399, 1998.

[4] R.J. Amdur and J.S. Bedford. Dose-rate effects between 0.3 and 30 gy/h in a normal and malignant human cell lines. *Int. J. Radiat. Oncol. Biol. Phys.*, 30:83–90, 1994.

[5] AmpTek, Unknown. X123 Energy Efficiency Table - Reference Manual.

[6] Park C. Barcellos-Hoff, M.H. and E. Wright. Radiation and the microenvironment - tumorigenesis and therapy. *Nature Reviews*, 5:867–875, 2005.

[7] Newton J.O. Beling, J.K and B. Rose. The decay of ^{241}am. *Phys. Rev.*, 87:670–671, 1952.

[8] Dolling J-A. Maves S.R. Siwarungsun N. Boreham, D.R. and R.E.J. Mitchel. Dose-rate effects for apoptosis and micronucleus formation in gamma-irradiated human lymphocytes. *Radiat. Res.*, 153:579–586, 2000.

[9] McKeever-S.W.S Botter-Jensen, L. and A.G. Wintle. *Optically Stimulated Luminescence*. Elsevier, 2003.

[10] McKeown C. K. Tucker J.D. Ljungquist S. Caldecott, K.W. and L.H. Thompson. An interaction between the mammalian dna repair protein xrcc1 and dna ligase iii. *Molecular and Cellular Biology*, 14(1):68–76, 1994.

[11] Bailey S.M. Cornforth, M.N. and E.H. Goodwin. Dose responses for chromosome abberations produced in noncycling primary human fibroblasts by alpha particles, and by gamma rays delivered at sublimiting low-dose-rates. *Radiat. Res.*, 158:43–53, 2002.

[12] Vidal S. Soleilhavoup J.P Vincent C. Serre G. Croute, F. and H. Planel. Effects of a very low-dose-rate of chronic ionizing radiation on the division potential of human embryonic lung fibroblasts *In Vitro. Exp. Gerontol.*, 21:1–11, 1986.

[13] Birnie Dunbar P., 1998. Crystal Structure of Al_2O_3: http://aml.arizona.edu/classes/mse222/1998/CORUNDUM/structure.htm.

[14] Radiation Effects Research Foundation, 2008. www.rerf.or.jp/glossary$_e$/*backgrou.htm*.

[15] E.J. Hall. *Radiobiology for the Radiobiologist.* Lippincott Williams Wilkins, 2005.

[16] Y. Ina and K. Sakai. Prolongation of life span associated with immunological modification by chronic low-dose-rate irrdation in mrl -lpr/lpr mice. *Radiat. Res.*, 161:168–173, 2004.

[17] Invitrogen, 2008. CyQUANT Protocol.

[18] Passell T.O. Browne C.I. Jaffe, H. and I. Perlman. Gamma and x-radiation in the decay of am^{241}. *Phys. Rev.*, 97(1):142–150, 1954.

[19] Nagasawa H. Weil M. M. Little J.B. Kato, T.A. and J.S. Bedford. Levels of γ-h2ax foci after low-dose-rate irradiation reveal a dna dsb rejoining defect in cells from human atm heterozygotes in two at families and in another apparently normal individual. *Radiat. Res.*, 166:443–453, 2006.

[20] Mohankumar M.N. Hamza V.Z. Kumar, P.R.V. and R. K. Jeevanram. Dose-rate effect on the induction of hprt mutants in human g_0 lymphocytes exposed *In Vitro* to gamma radiation. *Radiat. Res.*, 165:43–50, 2006.

[21] Ernest O. Lawrence Berkeley National Laboratory, 2000. http://ie.lbl.gov/toi/nuclide.asp?iZA=950241.

[22] S.W.S. McKeever. Optically stimulated luminescence dosimetry. *Nuclear Instruments and Methods in Physics Research B*, 184:29–54, 2001.

[23] Folkard M. Mitchell, C.R. and Joiner M. C. Effects of exposure to low-dose-rate ^{60}co gamma rays on human tumor cells *In Vitro. Radiat. Res.*, 158:311–318, 2002.

[24] James Mutamba, 2008. Presentation on Biological Function of XRCC1.

[25] Little J.B. Tsang N.M. Saunders E. Tesmer J. Nagasawa, H. and G.F. Strniste. Effect of dose-rate on the survival of irradiated human skin fibroblasts. *Radiat. Res.*, 132:375–379, 1992.

[26] Rebecca L. Raabe. Radiation effects on the blood-brain barrier. Master's thesis, Massachusetts Institute of Technology, 2007.

[27] Wang Rong. *Direct and indirect effects of alpha pArticle irradiations of human prostate tumor cells.* PhD thesis, Massachusetts Institute of Technology, 2005.

[28] J.S. Rubin and G.F. Whitmore. Dna repair-deficient chinese hamster ovary cells exhibiting differential sensitivity to γ rays under aerobic and hypoxic conditions. *Radiat. Res.*, 101:528–534, 1985.

[29] Hoshi Y. Nomura T. Oda T. Iwasaki T. Fujita K. Yamada T. Sakai, K. and H. Tanooka. Suppression of carcinogenic processes in mice by chronic low-dose-rate gamma-irradiation. *Int. J. Low Radiation*, 1:142–146, 2003.

[30] Kazuo Sakai, 2004. CRIEPI Newsletter 401 - Shedding Light on the Effects of Low-Dose Radiation.

[31] Lu L. Kaiser H. Shen, R.S. and H. Broxmeyer. *Eicosanoids and Other bioactive Lipids in Cancer Inflammation and Radiation Injury 3.* Plenum Press, 1997.

[32] Marples B. Matthews J. Joiner M Skov, K. and H. Zhou. A preliminary investigation into the extent of increased radioresistance or hyper-radiosensitivity in cells of hamster cell lines known to be deficient in dna repair. *Radiat. Res.*, 138:S126–S129, 1994.

[33] Landauer InLight Systems, Unknown. Description of μStar Dot Dosimetry System.

[34] K. Sakai *et al.* Suppressive effect of long-term low-dose-rate gamma-irradiation on chemical carcinogenesis in mice. *Internation Congress Series*, 1236:487 – 490, 2002.

[35] Brookman K.W. Dillehay L.E. Carrano A.V. Mazrimas J.A. Mooney C.L. Thompson, L.H. and J.L. Minkler. A cho-cell strain having hypersensitivity to mutagens, a defect in dna strand-break repair, and an extraordinary baseline frequency of sister-chromatid exchanged. *Mutation Research*, 95:427–440, 1982.

[36] K. W. Brookman N. J. Jones S. A. Allen Thompson, L. H. and A. V. Carrano. Molecular cloning of the human xrcci gene, which corrects defective dna strand-break repair and sister chromatid exchange. *Mol. Cell. Biol.*, 10:6160–6171, 1990.

[37] James E. Turner. *Atoms, Radiation, and Radiation Protection.* Wiley-VCH, 2007.

[38] Furuno-Fukushi I. Ueno, A.M. and H. Matsudaira. Induction of cell killing, micronuclei, and mutation to 6-thioguanine resistance after exposure to low-dose-rate γ rays and tritiated water in cultured mammalian cells (l5178y). *Radiat. Res.*, 91:447–456, 1982.

[39] Murray-D. vanAnkeren, S.C. and R.E. Meyn. Induction and rejoining of γ-ray-induced dna single- and double-strand breaks in chinese hamster aa8 cells and in two radiosensitive clones. *Radiat. Res.*, 116:511–525, 1988.

[40] Murray-D. Stafford P.M. vanAnkeren, S.C. and R.E. Meyn. Cell survival and recovery processes in chinese hamster aa8 cells and in two radiosensitive clones. *Radiat. Res.*, 115:223–237, 1988.

[41] M.M. Vilenchik and A.G. Knudson. Inverse radiation dose-rate effects on somatic and germ-line mutations and dna damage rates. *Proceedings of the National Academy of Science*, 97(10), 2000.

[42] Thierens-H. Vral, A. and L. DeRidder. Study of dose-rate and split-dose effects on the *in vitro* micronucleus yield in human lymphocytes exposed to x-rays. *Int. J. Radiat. Biol.*, 61(6):777–784, 1992.

[43] R.L. Wells and J.S. Bedford. Dose-rate effects in mammalian cells. *Radiat. Res.*, 94:105–134, 94.

[44] Nagasawa-H. Warner C.L. Fitzek M.M. Little J.B. Wilson, P.F. and J.S. Bedford. Radiation sensitivity of primary fibroblasts from hereditary retinoblastoma family members and some apparently normal controls: Colony formation ability during continuous low-dose-rate gamma irradiation. *Radiat. Res.*, 169:483–494, 2008.

[45] Jacquelin C. Yanch, 2008. DOE Low-Dose-Rate Project Grant Application.